Deep-Sea Research II 55 (2008) 1964–1987

Contents lists available at ScienceDirect

Deep-Sea Research II

journal homepage: www.elsevier.com/locate/dsr2

Western Antarctic Peninsula physical oceanography and spatio–temporal variability

Douglas G. Martinson [a,b,*], Sharon E. Stammerjohn [a,b], Richard A. Iannuzzi [a], Raymond C. Smith [c], Maria Vernet [d]

[a] Division of Ocean and Climate Physics, Lamont-Doherty Earth Observatory of Columbia University, 61 Route 9W, Palisades, NY 10964, USA
[b] Department of Earth and Environmental Sciences, Columbia University, New York, NY 10027, USA
[c] Institute for Computational Earth System Science and Department of Geography, University of California, Santa Barbara, CA 93106, USA
[d] Integrative Oceanographic Division, Scripps Institution of Oceanography, University of California San Diego, La Jolla, CA 92093-0218, USA

ARTICLE INFO

Article history:
Accepted 22 April 2008
Available online 13 August 2008

Keywords:
Antarctic Peninsula
Rapid climate change
Physical oceanography
Upper Circumpolar Deep Water
Ocean heat flux
Ocean-sea ice

ABSTRACT

This study focuses on 12 years of physical oceanography data, collected during the Palmer, Antarctica, Long-Term Ecological Research program (PAL LTER) over the continental margin of the western Antarctic Peninsula (WAP). The dataset offers the most long-lived consistent CTD-gridded observations of Antarctic waters collected anywhere in the Southern Ocean. The physical characteristics, water column structure and spatio–temporal variability of the various properties are examined for physically consistent and ecologically important patterns and modes of variability. Unique findings of note include: (1) The average annual ocean heat flux (to the atmosphere) over the continental shelf shows a *decreasing* trend through time averaging $0.6\,W\,m^{-2}\,yr^{-1}$, with an annual average ocean heat flux of $\sim 19\,W\,m^{-2}$. The ocean heat content over the shelf shows a linearly *increasing* trend of $2.6\times 10^{7}\,J\,m^{-2}yr^{-1}$, due predominantly to increased upwelling of warm Upper Circumpolar Deep Water (UCDW) onto the shelf with a small contribution due to a slight warming of UCDW (but over longer time scales (50 yr), the warming of UCDW dominates), (2) optimal multi-annual average vertical turbulent diffusivity coefficient (k_z) is $\sim 8.5\times 10^{-5}\,m^2s^{-1}$, determined by inversion considering warming of trapped remnant winter mixed layer water, (3) the water masses in the grid are well separated according to bathymetrically controlled features, dividing the sample domain into 3 sub-regions: slope, shelf and coastal waters; (4) the Antarctic Circumpolar Current (ACC) was *always* present along the shelf-break (consistent with the Orsi et al. [1995. On the meridional extent and fronts of the Antarctic Circumpolar Current. Deep-Sea Research I 42 (5), 641–673.] climatology) where UCDW shows its farthest southern extent and forms the Southern ACC Front (SACCF). The spatio–temporal variability of the delivery and distribution of ocean heat is dictated by the dynamics that are consistent with changes in the state of ENSO (La Niña drives enhanced upwelling in this region) and in the strength of the Southern Annular Mode (SAM; +SAM drives a local response similar to that of La Niña). The large 1997–1998 El Niño, followed by the transition to the strong La Niña of 1998–1999 (amplified by a large +SAM) introduced a regime shift on the shelf, resulting in the elimination of ~0.5 m of sea ice melt (presumably from the loss of sea ice being grown). 2002 was an anomalous year coinciding with an extraordinary storm forcing driving a 4.5σ increase in the heat content on the shelf. These jumps coincide with considerable changes in sea ice distribution as well. Pure UCDW on the shelf is primarily restricted to the deep canyons, with occasional appearances on the shelf floor near the middle of the grid. Anomalies in summer sea surface temperatures reflect wind strength (stronger winds mixing more cold winter water to the surface, with cooler SST; light winds, the opposite).

1. Introduction

Waters adjacent to the western Antarctic Peninsula (WAP) represent a unique mixture of circumpolar and shelf water processes. The region is of particular interest since it is an area undergoing the most extreme recent rapid regional warming on Earth (e.g., Smith and Stammerjohn, 2001; King et al., 2003;

* Corresponding author at: Division of Ocean and Climate Physics, Lamont-Doherty Earth Observatory of Columbia University, 61 Route 9W, Palisades, NY 10964, USA.
E-mail address: dgm@ldeo.columbia.edu (D.G. Martinson).

0967-0645/$ - see front matter © 2008 Elsevier Ltd. All rights reserved.
doi:10.1016/j.dsr2.2008.04.038

Vaughan et al., 2003; Turner et al., 2006). As such, it represents an end member whose understanding may prove useful for estimating changes that might occur elsewhere under a similar degree of warming (for example, it plays a major role in glacial melt and ecosystem change). These waters lie in close proximity to the Antarctic Circumpolar Current (ACC), and their influence on circumpolar waters circulated throughout the world's oceans is also of interest.

Infrequent hydrographic data have been collected in this region since the 1800s, starting with the expeditions of von Bellingshausen in 1821 and de Gerlache in 1889. More recently, annual data have been systematically collected through the Palmer Long Term Ecological Research program (PAL LTER; Smith et al., 1995) complementing the Antarctic Marine Living Resource (AMLR; http://swfsc.noaa.gov/textblock.aspx?Division=AERD) program from the mid-1980s, with new additions from the Southern Ocean GLOBal Ocean ECosystem Dynamics program (SO GLOBEC; Hofmann et al., 2002). The latter, in particular, have resulted in excellent descriptions of the regional water masses, stratification, etc.

This paper, focusing primarily on 12 years of PAL LTER data (1993–2004), aims to improve our documentation and understanding of how this system (or more broadly, the ocean–atmosphere–ice (OAI) system) *varies* in space and time throughout the WAP region. This is done through examination of the spatial and temporal distributions of primary water masses and their covariabilities. We focus on the central continental shelf region of the PAL LTER marine grid (separate from the daily sampled grid in the immediate vicinity of the Palmer US Antarctic research station, on Anvers Island).

2. Data

2.1. Analysis domain

The broad ocean domain of interest lies over the continental margin forming the eastern boundary of the Bellingshausen Sea, specifically within the PAL LTER nominal marine sampling grid (Fig. 1). The grid overlies a broad continental shelf averaging ~450 m in depth (excluding canyons); it runs ~200 km in cross-shelf width, and ~500 km along the WAP. Here, the southern boundary of the ACC flows over the slope along the shelf break, as it does throughout the entire SE Pacific region (Orsi et al., 1995) (Fig. 1A). The glacially sculpted (Anderson, 2002) coastline along the peninsula is highly convoluted, cut with numerous islands, deeps, fjords, submarine canyons, and a series of embayments often interconnected by channels ("inland passages" according to Hofmann et al., 1998), sometimes as deep as 900 m, but more typically o 450 m deep. The domain is divided into three sub-regions (Fig. 1B): continental slope, shelf and coastal regions—consistent with bathymetry, property distributions and ocean dynamics.

Stations are located on a grid system, delineated by "grid lines" that are 100 km apart and lie perpendicular to the average coast. Stations are spaced every 20 km along these grid lines across the shelf. Grid lines are labeled according to their position in the grid relative to the southern-most sample location; grid stations are labeled according to their cross-shelf distance from the average coast. Individual stations are identified as ggg.sss, where the ggg is the grid line and sss is the grid station location (e.g., station 600.080 lies 80 km offshore on the grid line 600 km up the

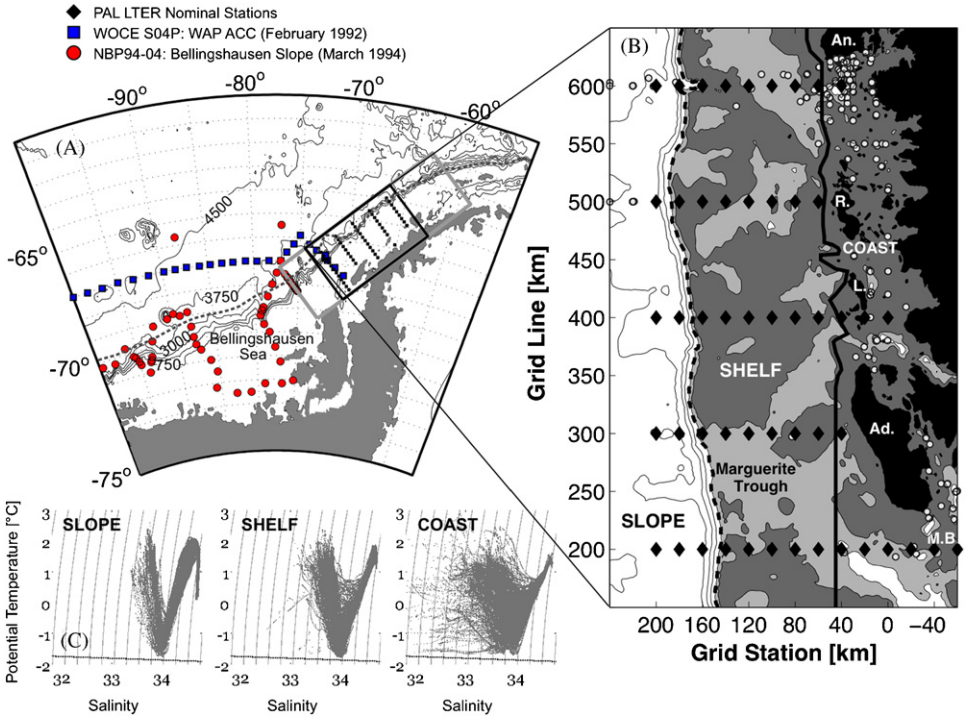

Fig. 1. (A) Study region along the WAP and nominal PAL LTER sampling grid (bold black box) imbedded in bigger full grid (bold grey box) with labeled contoured bathymetry (750-m intervals) and climatological southern edge of ACC (dashed grey line); hydrographic stations (small squares), the WOCE S04P section (blue squares), NBP94-02 section (red dots) over the Bellingshausen Sea shelf (and Amundsen Sea shelf off map to west). (B) Nominal sampling grid; bathymetry shaded (white X 750 m, 7504 light-greyZ 450 m, dark-grey o 450 m) and contoured (X 1500 m at 50 m intervals); islands labeled: An. = Anvers, R. = Renaud, L. = Lavoisier, Ad. = Adelaide; the 200 grid line extends into Marguerite Bay (M.B. on map); continental shelf break indicated by dashed bold line (slope to left) and shelf-coastal sub-regions separated by solid bold line; standard station locations (black squares) as well as numerous others occupied (small open circles) are indicated; grid lines (ordinate) and grid stations (abscissa) are indicated and labeled. (C) *T–S* diagrams for three bathymetric-controlled sub-regions (slope, shelf, coast indicated in B) where the bathymetry serves as geographic sieve, as evidenced by natural groupings of *T–S* diagram shapes: V-shape over slope where the water is continuously renewed by ACC; U-shape in coast sub-region where renewal is infrequent, and combination of shapes in transitional shelf sub-region.

peninsula from the southern-most line of the grid, starting near Alexander Island with 000.000 at ~69.01S, ~73.61W). The nominal sampling grid is confined to the 200–600 lines (highlighted in Fig. 1B), as those lines have the most consistent sampling. Other off-grid stations, such as those surrounding the immediate area of Palmer Station on Anvers Island are used when appropriate, and noted as such. The SO GLOBEC grid overlaps the southern section of the grid, southwest of the 300 grid line (Hofmann et al., 2002, their Fig. 2c).

Most of the stations indicated in Fig. 1B have been occupied each austral summer (typically the first week of January to early February) since 1993 (an initial survey cruise was conducted in November, 1991). The PAL LTER cruise data are supplemented and placed into a broader circumpolar context via: (1) comparison with hydrographical data collected throughout the Southern Ocean and primarily stored in the National Ocean Data Center (NODC) archives, in particular, the February 1992 WOCE S04P data (available in Orsi and Whitworth, 2005) and the March 1994 NBP94-02 data (Giulivi and Jacobs, 1997), and (2) passive and active microwave satellite observations placed on a larger "expanded grid" (Smith et al., 2008). The latter place the PAL LTER data into both temporal and spatial context with respect to sea ice (Smith et al., 1996, 1998b; Stammerjohn and Smith, 1997; Smith and Stammerjohn, 2001; Stammerjohn et al., 2003, 2008b) and regional-scale estimation of pigment biomass and phytoplankton productivity through ocean-color satellite observations (Smith et al., 1998a; Dierssen et al., 2000, 2002). Even though the WAP marine ecosystem displays large interannual variability in physical forcing, plankton biomass and primary production, persistent spatial patterns have been observed over the past 12 years of study (Smith et al., 1998b; Garibotti et al., 2003, 2005). The linkages observed between physical forcing and ecological response provide strong motivation for investigating the mechanisms that maintain these patterns at different time and space scales.

2.2. PAL LTER hydrography data

Ocean profile data (e.g., CTD, XBT, XCTD, optical properties, fluorescence) and bottle data at standard depths, including samples for chemical (nutrients) and biological data (phytoplankton, zooplankton, bacteria), as well as bird and marine mammal data, were collected each austral summer. Non-summer data were collected during special process cruises (November 1991, March and August 1993, June 1999 and September 2001). All data are available in the PAL LTER database (http://pal.lternet.edu/data/).

From 1993 to 1997, temperature (T) and salinity (S) data were obtained from an internally recording Seabird SEACAT system integrated into the Bio-Optical Profiling System (BOPS; Smith et al., 1984). Since 1998 (and for deep stations in 1996 and 1997) standard CTD data have been obtained through use of a SeaBird 911+ CTD system; dual pumped sensors have been used since 1999. These data are collected following our standardized CTD sampling procedures (Martinson et al., 1999). CTD sensors were pre- and post-cruise calibrated by SeaBird. Standard post-cruise calibration corrections were applied to the data, along with standard data reduction. Consistent, stringent quality assessment and control (qa/qc) of the T and S profile data were applied to all data (typically, standard statistical characterizations followed by detailed inspection of the individual profiles and groupings of profiles). For some analyses, additional profile examinations were conducted to make sure the data were consistent for the particular analysis. The results presented here are based on 1529 CTD station profiles (1173 from 12 summer cruises, 1993–2004; 356 from five non-summer cruises), but with particular focus on the extensive summer snapshots of the grid.

2.2.1. Nutrients

Water is drawn from 12-L Niskin bottles tripped on the upcast of the CTD while stopped in all major water masses and key water structure features. For nutrients, the samples were analyzed immediately after collection (within an hour at most), or if refrigerated, not longer than 2–4 h after collection; for longer storage, samples were frozen at −20 1C, later thawed in a warm water bath. Samples were analyzed for phosphate (except in January 1997), nitrate plus nitrite, nitrite, silicic acid and ammonium by segmented, continuous flow analyzers with an Alpkem Flow Solution IV system based on colorimetric methods and Softpac data collection software, January 1995–1998, 2000 and 2002–2005) or a Lachat QuickChem 800 flow injection nutrient analyzer (January 2005 and 2006). Samples were analyzed at the Marine Science Institute's Analytical Laboratory, Santa Barbara, CA using a Lachat QuickChem 800 flow injection nutrient analyzer on 4 cruises: January 1993, 1994, 1999 and 2001.

Comparison of nutrient determinations between onboard analysis and frozen samples analyzed at the MSI Analytical Laboratory, Santa Barbara, showed excellent agreement. The 1994–1996 nutrient data were noisier than later years.

For water mass analyses, two pseudo-conservative nutrient property values are defined: $N^* = [NO_3^-] - 16PO_4$ (Gruber and Sarmiento, 1997) and $Si^* = [Si(OH)_4] - [NO_3^-]$ (Sarmiento et al., 2004), which have been shown to be useful in the Southern Ocean.

2.2.2. Primary water masses

While properly suited for Section 4, the remainder of this paper is highly dependent upon local water mass descriptions, hence they are presented here. Key water masses, as they appear in T–S space for the austral *summer* WAP, are shown in Fig. 2, showing all

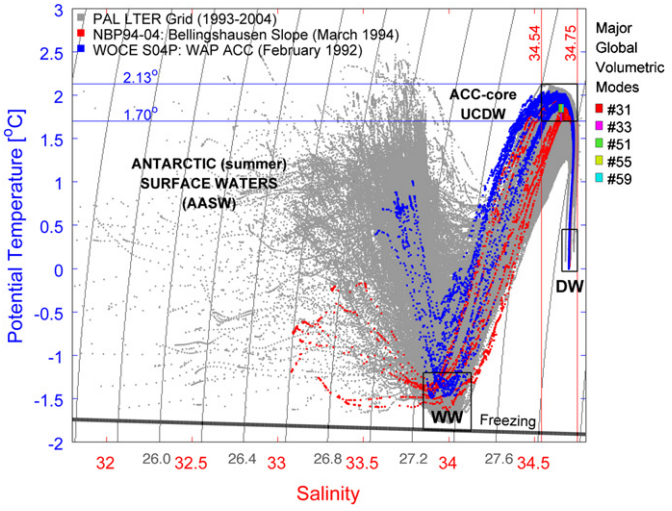

Fig. 2. θ–S scatter plot for 12 years of summer PAL LTER CTD station data (grey), February 1992 WOCE S04P data (blue) lying within 1000 km of the WAP region in waters deeper than 3 km (blue squares in Fig. 1A), and March 1994 NBP94-02 data (red) on the slope in the Bellingshausen Sea (small red dots in Fig. 1A) showing values of regional ACC-core UCDW (as it appears off-shelf of the WAP). Key water masses, as they appear in the WAP region, are indicated and labeled (UCDW = Upper Circumpolar Deep Water; WW = Winter Water; AASW = Antarctic Surface Water in summer; a local "end-member" deep water: DW). Also included within the UCDW box are five small water classes (small areas in θ–S space, following Montgomery, 1958), lying within 0.1 1C × 0.01‰ boxes.

of the LTER CTD profile data (most of the analyses involve waters shallow enough that use of potential temperature, θ, is not necessary, so it is used interchangeably with T).

The most prominent water mass in the Antarctic polar oceans, as noted by Deacon (1937), is the warm deep water (WDW, or, Circumpolar Deep Water, CDW). Over the broad circumpolar belt CDW spans a considerable range in T and S (sometimes given as any water warmer than 0 1C and saltier than 34.6). Gordon (1971a) distinguishes between Upper and Lower CDW, noting that these two water masses are characterized by core layers displaying temperature (UCDW) and salinity maxima (LCDW). Here, the separation of CDW is somewhat arbitrary; with LCDW playing no obvious role in this study, it is ignored (see dedicated discussion of LCDW in the southern portion of this grid in Klinck et al., 2004). The focus here is on UCDW, the dominant water mass that is quickly modified (cooled and freshened by mixing), forming modified UCDW (M-UCDW), as it moves across the shelf, away from its regional source over the slope (ACC-core UCDW).

In order to understand the relationship of shelf water masses to those of the ACC, UCDW is defined here by how it appears immediately offshore of the WAP shelf (i.e. as it is delivered to the region). For this, two nearby cruises that clearly sampled ACC waters are used: (1) the February 1992 WOCE S04P section, focusing on profiles taken in deep water within 1000 km of the WAP shelf, and (2) the March 1994 NBP94-02 section (Giulivi and Jacobs, 1997) over the Bellingshausen Sea slope. θ_{max} waters (i.e., UCDW) at these stations occupy a rather restricted area in θ–S space, shown by the UCDW box in Fig. 2, as 1.70p θp 2.13 1C; 34.54p Sp 34.75. Within this box lie five small water classes (small areas in T–S space, following Montgomery, 1958), lying within 0.1 1C × 0.01‰ boxes. Worthington (1981) shows that these classes represent major global ocean volumetric modes. Specifically, of nearly 700 classes, the five shown in Fig. 2 rank as 31, 33, 51, 55 and 59 of the most voluminous water masses. The bulk of the waters within these classes reside in the South Pacific, with lesser amounts occurring in the North Pacific.

Quantification of circumpolar water masses has grown primarily from the Atlantic sector where early oceanographic explorations were located and where the CDW is most influenced by upwelled North Atlantic Deep Water (NADW) entering the ACC (e.g., Wust, 1933; Mosby, 1934; Reid et al., 1977; Gordon, 1971a, b; Carmack, 1977). More detailed analyses of the Southeastern Pacific that encompasses the WAP region can be found in Gordon (1971a), Hofmann et al. (1996), Smith and Klinck (2002) and Klinck et al. (2004). The definition of UCDW used here (as described above) is more restricted than others but is most similar to that of Klinck et al. (2004), defined for the waters within the SO GLOBEC grid. This distinction is necessary in order to differentiate circumpolar-scale variability from local WAP variability (the former seems small considering the volumetric mode locations in Fig. 2).

Winter Water (WW; Mosby, 1934)—the T_{min} layer according to Mosby (who devoted considerable discussion to its formation, something that was still controversial in his time)—is also prevalent throughout the Antarctic polar waters, in fact, *defining* polar waters (Gordon, 1971b). WW is the T_{min} water, but this is loosely defined in Fig. 2 as T_fp Tp −1.2 1C; 33.85p Sp 34.13 (cf. Mosby's average summer values of −1.69 1C and 34.33‰). It is formed at, or within millidegrees of, the freezing point during autumn–winter (Toole, 1981), so that in winter, the entire surface mixed layer is WW. During summer, the temperature of the remnant *winter* mixed-layer water is well above freezing due to vertical mixing with warmer waters bounding it above and below; the surface water goes by the clever name of Antarctic Surface Water (ASW).

Table 1
Defining characteristics of fundamental end-member water types (WW, UCDW, DW)

Water type	T (1C)	S	Si*	N*
WW	−1.8587 0.004	33.8807 0.062	39.537 3.20	−3.267 0.41
DW	0.4167 0.029	34.7077 0.003	105.747 5.60	−0.347 1.92
UCDW 1998	2.0367 0.055	34.6557 0.020	47.617 4.74	−5.567 1.35
UCDW 1999	1.6837 0.229	34.5747 0.073	42.757 12.63	−4.657 2.71
UCDW 2000	1.8527 0.231	34.6697 0.030	55.437 8.01	−0.397 0.79
UCDW 2001	1.8577 0.270	34.6447 0.040	50.277 6.24	0.167 0.80
UCDW 2002	1.9857 0.105	34.6387 0.020	50.377 1.65	−2.637 2.68
UCDW 2003	1.9327 0.108	34.6897 0.023	52.897 7.06	0.627 0.56
UCDW 2004	1.8367 0.129	34.6877 0.022	57.097 6.45	−0.557 1.20

Here Deep Water (DW) is defined as a local deep water, the deepest water on the slope, forming an end-member in T–S space (Fig. 2), necessary for water mass mixing.

Defining property values of these key water types are presented in Table 1.

The most conspicuously absent Antarctic water masses on the WAP shelf are the low- and high-salinity shelf waters (LSSW, HSSW) found at depth over numerous shelf locations around the continent (Carmack, 1977). Those waters, near the freezing point, with 34.6 salinity separating LSSW from HSSW, are notable for their role in deep water and bottom water formations (Gill, 1973). Here the shelf bottom is bathed in UCDW derivatives; the coastal sub-region has bottom waters that are typically 31 above the freezing point. This is consistent with the notion that bottom waters do not form in the WAP region (e.g., Hofmann and Klinck, 1998).

2.3. Satellite sea-ice data

Sea-ice concentration data are from the SMMR-SSM/I time-series derived by the Goddard Space Flight Center (GSFC) Bootstrap passive microwave algorithm (Comiso, 1995) and are provided by the EOS Distributed Active Archive Center (DAAC) at the National Snow and Ice Data Center (NSIDC), University of Colorado in Boulder, Colorado (http://nsidc.org). A detailed description of the algorithm is given by Comiso et al. (1997). The sea-ice concentration data are mapped to a 25 × 25-km grid on a polar stereographic projection (NSIDC) and include a landmask and latitude/longitude pairs for geolocating pixels. Stammerjohn et al. (2008b) provide detailed sea-ice analyses relevant to the physics presented here; they also confirm that their results are consistent with those presented by Parkinson (2002) who used NASA Team derived sea-ice concentrations, indicating that the method (based on ice-edge detection) is not overly sensitive to algorithm choice.

3. Methods

The relationship of circumpolar waters to extrapolar climate has been well documented (e.g., White and Peterson, 1996; Yuan and Martinson, 2000, 2001; Hall and Visbeck, 2002; Martinson and Iannuzzi, 2003; Liu et al., 2004; Lefebvre et al., 2004), so here the focus is on WAP water-mass distributions, climatologies and the spatio–temporal variability about those climatologies. Specific focus is on the waters of the continental shelf and slope sub-regions (Fig. 1B), away from the complexities of glacial melt in the more convoluted coastal sub-region (which is receiving a more detailed analysis in a separate work).

3.1. Optimal Multiparameter (OMP) water-mass analysis

In an attempt to understand mixing on the continental shelf, and water-mass origins, optimal multiparameter (OMP) analysis is employed where possible and practical (comparable to that described by Tomczak and Large, 1989, though differing by not using their normalizations). This is a constrained weighted optimization where water masses are described in terms of the fractional composition of a set of fundamental (end-member) water types present in the region. Waters that may have been modified through exchanges with the atmosphere disobey OMP requirements that water properties reflect conservative mixing from the fundamental water types, restricting use of this method to waters below the permanent pycnocline. For those deep waters, we define fundamental water types by their S, N* and Si* property signatures; T is not conservative due to diffusive heat loss. Weights are defined according to the realized spread in property values in the region for the particular water type. Given its dependence on nutrients, this analysis can only be applied to depths where water-bottle data were collected, limiting the vertical resolution. Also, as discussed in Section 2, nutrient problems render the use of 1993–1996 Si data questionable in this context (tests indicate that the OMP results were severely sensitive to slight changes in the uncertainties used as weights for those years) and the absence of phosphate data in 1997 also yield that year unusable for this OMP analysis. So OMP analysis is restricted to the last 7 years: 1998–2004 only.

The OMP solution is easily determined by minimizing: $\mathbf{wAx} = \mathbf{wb}$, where *property matrix* **A**, is an $(m{+}1) \times n$ matrix, where m is the number of conservative water properties used to define the fundamental water types (here, $m = 3$: S, N* and Si*). The additional row (the +1) is unity, for mass conservation. The n columns are for the n fundamental water types present in the region that mix to form any water mass observed. Here, $n = 3$ (as discussed above, there are 3 fundamental water types: WW, Upper Circumpolar Deep Water (UCDW), and DW, with properties given in Table 1). So, column one contains the S, N*, Si* and 1, describing the first water type (in this case, WW). The other $n-1$ columns contain the same information in the same order for the other water types. Vector **x** is dimension n and is solved to give the fractional contribution of each of the fundamental water types (x_i) for the sampled water at each bottle depth. The weight matrix, **w**, is diagonal, with weights $1/\hat{\sigma}_\kappa$, where $\hat{\sigma}_\kappa$ is the sample standard deviation for property κ across the grid in a single year; the weight for the conservation row is a very large number, assuring that conservation is obeyed. Vector **b** is the vector containing the m properties of the water sample being decomposed, and 1 for conservation.

The system employs a nonnegativity constraint of the form: $\mathbf{Ix} \geq \mathbf{0}$, where matrix **I** is the identity matrix, forcing each fractional contribution (elements of **x**) to be nonnegative. As usual for inequality constrained equations, the system is first solved without constraints to see if they are needed. If required for a station, the inversion is rerun using the constraints. Constraints are generally required at locations where noise in the sample may be particularly large or the n fundamental water types may not be sufficient to properly define the observed water mass; we examine such locations to determine if there is spatial coherency suggesting a region that may, for example, require an additional water type. We also determine which water property requires the constraint, to help assure that properties are correctly defined for the fundamental water types.

Uncertainties in the fractional contribution, i.e., the elements of vector **x**, are found in the standard manner: $\mathrm{Var}[\mathbf{x}] = \mathrm{Var}[\mathbf{Cb}] = \mathbf{C}\mathsf{R}_\mathbf{b}\mathbf{C}^\mathrm{T}$, where $\mathbf{C} = [\mathbf{A}^\mathrm{T}\mathbf{w}^\mathrm{T}\mathbf{w}\mathbf{A}]^{-1}\mathbf{A}^\mathrm{T}\mathbf{w}^\mathrm{T}\mathbf{w}$, the pseudo-inverse, and $\mathsf{R}_\mathbf{b}$ is the (auto)covariance matrix for the sampled water. Var[**x**] ignores the nonnegativity constraint, giving a conservative estimate of variance for the fractional contributions (i.e., if the uncertainty allows the estimated fraction to be negative, it must be *reduced* in size to avoid this, giving a smaller uncertainty). We estimate $\mathsf{R}_\mathbf{b}$ through use of a data matrix, **D**. For each year, the **b** vector elements (1 vector per station, for the same bottle depth) as anomalies about their mean, are placed as columns in **D** for the region or sub-region of focus (typically the shelf). Then $\mathsf{R}_\mathbf{b} = M^{-1}\mathbf{D}\mathbf{D}^\mathbf{T}$, where M is the number of stations (columns) in **D**. This gives a reasonably estimated spatial covariability, appropriate here because of the pseudo-conservative nature of the n properties. Note that this approach gives only one uncertainty estimate per year (same value for all stations), since this estimate of the covariance matrix eliminates individual station covariabilities.

3.2. Upper ocean bulk property parameters

While standard ocean variables (e.g., T and S) have obvious intuitive appeal, in regions dominated by vertical processes, working with bulk parameters based on vertically integrated property distributions provide robust characteristics that are climatically meaningful in the sense of OAI interactions. Such integrated bulk properties are derived from the system scalings of Martinson (1990) and defined in Martinson and Iannuzzi (1998; hereafter MI98). The scalings show a primary regulation of the ocean-ice interaction by the mixed-layer T, S and depth, and vertical gradients of T and S ($\nabla_\mathrm{p}T$ and $\nabla_\mathrm{p}S$) through the permanent pycnocline. MI98 show that variance-stabilizing vertical integration of relatively long-lived information contained within the upper-ocean structure (T and S profiles) provides bulk property distributions, which are used directly, or in combinations, to provide fundamental OAI information such as ocean heat flux, overall water-column stability and sea-ice growth constraints.

This bulk property methodology was developed for the open ocean of the Weddell Gyre where the system was clearly dominated by vertical processes. As stated in MI98, vertical balance could not be assumed for the Weddell Gyre's narrow shelves, where strong lateral property gradients and currents were apparent. However, for the very broad and deep shelf of the WAP, the weak lateral property gradients, slow lateral current speeds (Moffat et al., 2005; Beardsley et al., 2004) and modeling work of Klinck (1998) and Smith and Klinck (2002) indicate that the system on the WAP shelf is predominantly controlled by vertical processes allowing application of the bulk property methods here. The method has been successfully applied in analyses of Antarctic as well as Arctic waters (Martinson and Steele, 2001), and as described in MI98, the winter bulk properties are well estimated from summer profiles.

3.2.1. Integration limits

Key to the bulk parameter methodology is an ability to identify integration depths from the summer profiles—specifically, the upper (top) and lower (bottom) limits of the seasonal and permanent pycnoclines (z_sm, z_sc, z_wm and z_wc; Fig. 3); the upper limits represent depths of the summer and winter mixed layers (z_sm, z_wm). By the time data is collected in mid-summer, z_sc and z_wm have been smeared by mixing.

The following method is employed to best estimate these depths. The measured summer profile at each station is manipulated (modeled) by eliminating heat (above freezing, T_f) from the upper meter of the water column and mixing downward with underlying waters until a hydrostatically stable profile is achieved. This describes a new mixed layer, and the difference between the salinity (S^m) of this new mixed layer and the actual S

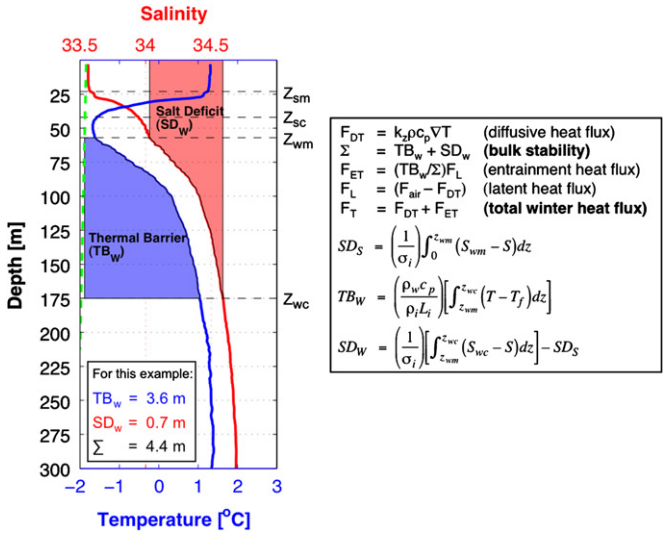

Fig. 3. Graphical depiction of computation of bulk property estimates of *winter*-average vertical ocean sensible heat flux (F_T) and bulk stability (R) from a summer profile. Blue shaded region on temperature profile shows thermal barrier; red-shaded area on salinity profile shows salt deficit. These and other characteristics of the profiles (mixed layer *T*, *S* and depth, and vertical gradients of *T* and *S* through the permanent pycnocline, ∇T and ∇S) are combined to provide climatically meaningful parameters, some of which are shown in the box to the right of the panel. Green dashed line is freezing point of seawater as function of the salinity and depth of profile. Formula for computing thermal barrier (TB_w), salt deficit (SD_w) and bulk stability (R) given in the lower box on right, and actual values for this particular profile are given as inset on profile-graph in lower left, in units of equivalent *in situ* sea ice thickness. Critical integration depths for the bulk properties are indicated on graph's right-side ordinate.

at the depth of the new mixed layer forms a new variable S^*. Heat is then removed from this mixture and the downward mixing continued in this iterative manner until no more mixing can be accomplished by cooling, and the mixture is at the freezing point. Then enough ice is grown in order to mix into the next depth step. The process is repeated until the entire profile is exhausted (see MI98 for further details on the entire method), yielding a profile of $S^*(z)$.

z_{wc} is defined as the depth at which mixing to the profile bottom occurs without further ice growth as the mixing breaks into the nearly neutrally stratified deep water. Because the mixing occurs at the freezing point, nonlinear terms in the equation of state (particularly, cabbeling and thermobaricity) enhance the depth of mixing such that z_{wc} is a stable estimate of the depth of the base of the permanent pycnocline (as in Fig. 3) and is the threshold of water-column static stability (a bifurcation in the system). When erosion (entrainment) of the winter mixed layer reaches this point, deep convection ensues, venting most of the heat remaining in the water column (generating a polynya if ice covered). This homogenizes the entire water column and dramatically changes the nature of the ocean-ice interaction at which point these bulk properties and the scalings of Martinson (1990), no longer apply; the entire vertical balance is altered until the water column can be restratified—typically via a large input of fresh water such as can occur via in-drifting sea ice or glacial meltwater.

$S^*(z)$ exaggerates the features of interest and has proven robust for defining z_{sc} and z_{wm}. These critical depths are defined on S^* as a penalty function: rewarded for high local, smoothed, curvature (seeking a local maximum, expected upon entering or departing from a mixed layer), penalized by moving closer to $S(z_{wc})$, an end member in salinity most different from that expected in the mixed layer (the penalty required to avoid selecting a fine layer intrusion with overall maximum curvature). z_{sm} is calculated in a similar manner, and while it tends to be less robust than z_{sc} and z_{wm},, it is not used as an integration limit. This method also provides an approximation of the winter profile that will be attained at the beginning of winter and seems to be a reasonable estimate of the preceding winter's end as well.

Computer code allowing reproduction of these picks and PDFs of the papers referenced for this methodology are available at http://www.ldeo.columbia.edu/~dgm/MartinsonLTERDSR.

MI98 devote considerable discussion to the assessment of the uncertainties associated with these integration depth picks and their impact on the bulk parameters. Analysis of these errors in the WAP (and of the parameters themselves) suggests that the parameter values and their uncertainties are comparable to those of the Weddell Gyre open ocean. For the WAP, the yearly averages of these picks by sub-region are presented as time series in http://www.ldeo.columbia.edu/~dgm/MartinsonLTERDSR.

3.2.2. Thermal barrier and salt deficit

Because polar oceans are characterized by cold, fresh waters overlying warmer, saltier waters, two bulk properties dominate and are easily determined once the integration depths are defined as described above; others are derived from them. Foremost is the available thermal energy, presented here as a winter "thermal barrier" (TB_w). This is the enthalpy relative to the freezing point (T_f) available within the permanent thermocline (Fig. 3, shown as picked from a summer profile). Second is a winter "salt deficit" (SD_w), the freshwater surplus in the upper ocean relative to the deep water (corrected for the nonlinear equation of state and vertical salt flux).

SD_w is reduced by salt input that works to destabilize the surface layer, driving mixing with the underlying deeper waters during mixed layer expansion. TB_w is the sensible heat that must be vented during erosion of the pycnocline, accompanying complete elimination of SD_w. Over the winter sea-ice growth period, for a mostly vertically driven system, SD_w is reduced by salinization (brine rejection) during sea-ice growth, driving an entrainment heat flux that vents TB_w, freshening and re-stabilizing (to some degree) the surface layer through sea-ice melt. TB_w thus provides a negative feedback to the ice growth-driven destabilization process, and in combination with the diffusive ventilation of ocean heat, reduces the sea-ice growth. Through these processes, the ocean heat dominates the otherwise statically weak Antarctic water column, preventing overturn in winter.

These bulk parameters are conveniently provided in terms of equivalent *in situ* sea-ice growth (reported in terms of ice thickness), as this growth is the primary means of destabilization and sea ice is an easy to measure or estimate observable in the field. The integral in Fig. 3 for TB_w is multiplied by $\rho_w c_p/\rho_i L_i$ (Table 2 defines constants) converting from units of m1C to an equivalent thickness of sea ice; likewise, the salinity integral is divided by σ_i, a constant converting an ice growth rate to a salt flux (assuming sea-ice salinity = 5‰). As such, SD_w reveals the thickness of *in situ* ice growth required to eliminate the surface freshwater surplus. TB_w reveals the thickness of overlying ice that could be melted (or prevented from growing) by completely venting the thermocline, and it indicates the potential to *resist* overturn, usually dominating SD_w by a factor of X 2 in Antarctic

Table 2
Coefficients used throughout text and in all computations

ρ_w (water density)	1027.5 kg m^{-3}
c_p (heat capacity of water)	4.00×10^3 J/(kg 1C)
ρ_i (sea-ice density)	900 kg m^{-3}
L_i (latent heat of fusion of sea-ice)	3.34×10^5 J kg^{-1}
S_i (converts sea-ice growth rate to salinity flux)	30‰

waters (in both the Weddell gyre and WAP). Summer salt deficit (SD_s) is calculated as described below and is the amount of autumn sea ice that must grow in order to eliminate the seasonal halocline (dominated by the spring/summer ice melt-layer).

3.2.3. Bulk stability

The most notable combination of SD_w and TB_w occurs in the form of bulk water-column stability (R), where $R = TB_w + SD_w$. This measure of stability indicates the amount of *in situ* ice growth (or its heat loss equivalent) sufficient to break down the permanent pycnocline and drive overturn (ignoring storm influences, which MI98 estimate can be large, but typically is small; in the extreme, extensive storms can vent TB_w without impacting SD_w, reducing R to SD_w only). The brine rejection associated with ice thickness of R causes mixing down to the point where the water column is statically unstable (a point of no return), driving catastrophic overturn, with mixing well into the deep water, if not to the bottom, imposing a stratification "regime shift" with likely polynya formation and potential long-term consequences (e.g., Martinson, 1991).

3.2.4. Summer salt deficit

For the summer water column, one of the more important and meaningful bulk property parameters is the SD_s. This is the amount of excess freshwater in the surface layer (from the surface down through the seasonal halocline) relative to that of the WW. As such, it is a measure, predominantly, of the amount of sea ice (with snow cover) that melted in the surface layer at the end of winter, responsible for generating the seasonal pycnocline and transitioning the water column into its summer configuration. This initial summer configuration marks a "time zero" for the biology seasonal cycle. In coastal regions, glacial melt also may contribute to this freshwater signal.

The seasonal pycnocline buffers the surface from the heat of deep water, so that during autumn, when the surface layer cools to freezing, the amount of ice growth required to eliminate the seasonal halocline is equal to SD_s. Once this amount of ice grows (typically within a few days during the intense cooling of the uninsulated ocean in the cold autumn), the seasonal pycnocline is removed. This initiates the strong winter heat flux across the permanent pycnocline such that the ocean sensible heat achieves a balance with the air–sea heat loss and little-to-no net ice growth is realized beyond SD_s. Hence, SD_s is a reasonable indicator of the upcoming winter ice-cover thickness, with some correction attributed to ice divergence (the difference in SD_s between consecutive years represents the net freshwater flux into or out of the area and provides some insights to upwelling). Note that SD_s can also include freshwater from other sources. The exact nature of the source is not relevant to the computation of SD_s; this value still represents the amount of sea ice that will have to form to eliminate the seasonal pycnocline, establish the winter mixed layer and initiate the strong winter heat flux. We are using inversion techniques in an attempt to differentiate various sources (sea ice, glacial and P–E) in SD_s elsewhere.

3.3. Ocean heat flux

3.3.1. Ocean sensible heat flux via bulk properties

The vertical ocean sensible heat flux is composed of two parts from a mechanistic ice-ocean interaction perspective: (1) a turbulent diffusive heat flux (F_{DT}), and (2) an entrainment heat flux (F_{ET}). F_{DT} operates year-round and is estimated in the standard manner: $F_{DT} = \rho c_p k_z \nabla T$, where k_z is an optimal seasonal turbulent diffusivity coefficient. An optimal *seasonal* value is required to take into account the orders of magnitude changes in k_z associated with the passage of storms, as shown by Stanton (personal communication) during the AnzFlux program (McPhee et al., 1996). F_{ET} operates during the winter, reflecting the sensible heat flux induced by entrainment (erosion) of the permanent thermocline during convective deepening of the winter mixed layer driven by densification from brine rejection during ice growth.

k_z is estimated by recognizing that a thickness (H_{WW}) of winter mixed layer water (WW) is trapped at the freezing point and then warmed above freezing (a change of DT_{WW}) by mixing across the permanent ($\nabla_p T$) and seasonal ($\nabla_s T$) thermoclines. The latter changes with summer surface warming, requiring a seasonal average value. Warming of this WW occurs over a known time interval (Dt_j; the elapsed time between spring melt and sampling time for station j). So, $DT_{WW} = [k_z|\nabla_p T| + k_z|\nabla_s T|](Dt_j/H_{WW})$. This is easily inverted for the most consistent (optimal) k_z. Because of noise in the system, all shelf and slope stations in a single year are used to optimize for one k_z per year, assuming that the region in general is subjected to the same surface stress throughout the season. This optimal solution is more reasonable than the average of noisy individual exact solutions at each station.

H_{WW} is derived from summer values as the thickness from z_{wm} (described above) to the bottom of the spring meltwater layer, z_{sc}. Because the latter is needed when it first forms (trapping WW at T_f) it is estimated from Large et al.'s (1994) KPP one-dimensional ocean mixing model. Initial conditions for each station consist of the estimated winter profile prior to the summer sample (as described above). This winter profile is then subjected to a surface freshwater flux: *in situ* sea-ice melt (thickness given by SD_s) applied over the time of ice melt (based on satellite observations of the timing of the spring sea-ice retreat, consistent with Stammerjohn et al., 2008b), with mean springtime surface winds (including average storms randomly appearing over the melt period). The model estimates the depth of the spring melt layer (z_{sc}; prior to its being mixed further over the summer before the water column is sampled). So, $H_{WW} = |z_{wm} - z_{sc}|$; its uncertainty is evaluated in the results section and tracked into that of k_z and F_{DT}. The model forcing is adjusted to yield mixed-layer conditions most consistent with those observed at the time of sampling, giving the change in $\nabla_s T$ (seasonal thermocline) over the warming period for the inversion. We find from this that the best estimate of an average $\nabla_s T$ (which progresses from zero to its solar insolated value at the time of sampling) is ~50% of the sampled value.

The entrainment flux during winter is given by $F_{ET} = TB_w/R)(\bar{F}_{air} - F_{DT})$, where $\bar{F}_{air}$ is taken from Large and Yaeger (2004) as 32.5 W m^{-2} average over the grid for all years. This is consistent with our sparse meteorological measurements, but a non-varying $\bar{F}_{air}$ is something limiting all such calculations, especially in light of a warming WAP that may lead to a decreasing $\bar{F}_{air}$. $\bar{F}_{air} - F_{DT}$ is the latent heat flux associated with freezing; this ice growth, whose brine release drives convection, releases more sensible heat from the thermocline proportional to TB_w/R. Any steady upwelling flux is subsumed by F_{ET}, since upwelling serves to raise the pycnocline, influencing TB_w and R.

Total *winter* average vertical ocean heat flux,

$$\begin{aligned} F_T &= F_{DT} + F_{ET} = F_{DT} + (TB_w/R)(\bar{F}_{air} - F_{DT}) \\ &= (TB_w/R)\bar{F}_{air} + F_{DT}(1 - TB_w/R) \\ &= (TB_w/R)\bar{F}_{air} + F_{DT}(SD_w/R). \end{aligned}$$

The uncertainty (as a variance) is

$$\begin{aligned} \mathrm{Var}[F_T] = \mathrm{Var}[(TB_w/R)\bar{F}_{air}] + \mathrm{Var}[F_{DT}(SD_w/R)] \\ + 2\,\mathrm{Cov}[(TB_w/R)\bar{F}_{air}; F_{DT}(SD_w/R)]. \end{aligned}$$

All variables in this expression are random variables, but because some terms lead to nonlinear terms in expectancy, we estimate the uncertainties of the terms (as products and ratios) instead of linearizing the terms for expectancy and tracking the impact of individual uncertainties.

This method of determining F_T works well in capturing the average winter heat fluxes. For example, estimates of winter-averaged bulk parameter-derived heat fluxes for the central Weddell Gyre region were corroborated by comparing them to time-averaged measured fluxes (McPhee et al., 1999) for the same location measured over the entire winter during the 1994 Weddell AnzFlux program (McPhee et al., 1996): measured and bulk parameter estimates agree to better than $2\,W\,m^{-2}$ (for a winter-average flux of $\sim 29\,W\,m^{-2}$).

An annual average ocean heat flux is defined by: / F_{ann}S = (Dt_w/365)F_{ET}+F_{DT}, where Dt_w = ice-covered time at the particular station (period where sea ice and winter mixed layer are present, so both entrainment and diffusive heat fluxes active); the diffusive heat flux is active year-round.

3.3.2. Ocean sensible heat flux via changed heat content

Alternatively, the annual ocean heat flux is estimated as the change in ocean heat content (Q) over a year time span (Dt_{yr}), so, $F_{ann} = DQ/Dt_{yr}$. The heat content of relevance on the shelf is the sub-WW (from z_{wm} down 300 m), defined here as

$$Q_k = \sum_{X_k} \left[\int_{z_{wm}}^{z_{wm}+300} \rho c_p [DT_f(z)]\, dz \right],$$

where $DT_f = T - T_f$ and X_k is for all stations in sub-region, k. The sub-WW 300 m depth range accounts for most of the heat on the shelf while excluding the least number of stations for being too shallow.

The estimate of F_{ann} is limited by a lack of knowledge of the frequency and extent of ACC flooding events of the shelf (providing the source of heat in UCDW). Klinck et al. (2004), using current meter data in the southern portion of our grid, note that they see the start of several flooding events within Marguerite Trough over their March–April and July–August observation periods, but how thoroughly the shelf is flooded each event is unclear. One complete flooding of the shelf per year is assumed here as a starting point.

Two methods of estimating the change in heat content from its initial value offshore are possible: (1) The heat content of the shelf deep waters, Q_{shelf}, began offshore as Q_{slope}, the heat content of pure UCDW over the slope the *previous* year (i.e. the heat delivered to the region by the ACC at the start of the year), so that the change from slope to shelf value ($DQ_{shelf}^{total\,Q}$) is the change in heat content. (2) The change in heat content *not* associated with mixing and given by the difference in the observed Q and that Q explained by mixing, as given by the OMP fractional mixing vector, **x**. A similar calculation is used to determine the amount of Q associated with the physical mixing (entrainment) of WW into UCDW (fraction of WW contained in M-UCDW).

For the first approach, the change in heat content for each year is converted to an annual ocean heat flux F_{ann} as follows: $DQ_{shelf}^{total\,Q} = F_{DT}Dt_s + F_T Dt_w$, but since $F_T = F_{DT}$+F_{ET}, $DQ_{shelf}^{total\,Q} = F_{DT}Dt_{yr} + F_{ET}Dt_w$. This is easily placed in standard matrix (**Ax** = **b**) form for an optimal multi-year annual average ocean heat flux / $F_{ann}$$S_{Q-11}$ (note that since DQ involves Q_{slope} from the previous year, this allows only 11 years of DQ estimates). **A** is an 11×2 matrix, with each row containing Dt_{yr} and Dt_w for that particular year (Dt_{yr} being the time since last flooding event—here 1 year; Dt_w the length of winter leading up to that particular sample season), and vector **b** containing the 11 annual $DQ_{shelf}^{total\,Q}$ values, so that **x** gives the optimal F_{DT} and F_{ET} from this changing heat content approach. This value of change in heat content is overestimated, since some of the change is due to physical mixing, and underestimated if there is more than one full shelf flooding event per year.

The second approach recognizes that some of $DQ_{shelf}^{total\,Q}$ is associated with simple mixing (i.e., pure UCDW is cooled to M-UCDW by mixing with the colder WW and DW). We wish to isolate that component of $DQ_{shelf}^{total\,Q}$ not due to mixing of water types. This is determined through our OMP results that provide the fraction of mixing with WW and DW (given by mixing vector **x**). To obtain the cooling *not* attributable to mixing, $DQ_{shelf}^{DT-loss}$, new property matrix, $\mathbf{A_T}$, is constructed that includes the defining temperature of each water type (something not included in the original **A** property matrix). From this, $\hat{b}_{mix} = \mathbf{A_T x}$, where $\hat{\mathbf{b}}_{mix}$ is a best-fit vector describing the water properties for each hydrographic bottle in the sub-WW layer. Since $\mathbf{A_T}$ includes temperature, $\hat{\mathbf{b}}_{mix}$ will provide an estimate of the temperature (T_{mix}) expected from the mixture that best satisfies all of the other properties used to define the fundamental water types. The difference between the temperature expected from mixing and that observed (T_{obs}), $DT_{DT} = (T_{obs} - T_{mix})$ is attributed to reduced T via F_{DT}. So, $DQ_{shelf}^{DT-loss} = \sum_{X_k}\{\sum_b h_b \rho c_p [DT_{DT}(z)]\}$, where the inner integral has been replaced by a sum over the **b** discrete water bottle samples occurring in the deep water; each bottle is assumed to be representative of a depth range h_b, which spans half the depth to each of the neighboring bottles. A similar approach can be used to determine the cooling associated with mixing (entrainment) of WW mixed into the underlying sub-WW layers, giving the entrainment change in Q.

Unfortunately this second approach suffers from degraded vertical resolution and failure of the method in cases where x_{UCDW} o 50% (for the diffusive value) and x_{WW} 4 50% (for the entrainment value). These problems render this approach more difficult so only the first approach ($DQ_{shelf}^{total\,Q} = Q_{slope} - Q_{shelf}$) is employed in this study.

3.4. Climatologies (spatial variability)

Climatologies (mean multi-year values) of physical properties and bulk parameters as a function of location are calculated on a grid consistent with the station distribution (grids make equal area rectangles surrounding each station with the cell boundaries at the half-way point between the closest neighboring nominal stations). Climatologies are produced by averaging all values within a grid cell for a single year and then averaging all of the yearly averages within the cell. The sensitivity of the climatology to methodology is tested by forming other climatologies using: (1) the average of all values, regardless of year (thus biasing the average to those years with more samples in a grid cell), and (2) the median (instead of the mean). These sensitivity tests produced no meaningful differences (other than obvious statistical ones).

3.5. Interannual variability and principal component analysis

Evaluating the interannual variability (about the climatologies) and its spatial structure provide a means for examining spatio–temporal variability and the covariability and interactions between different properties and parameters throughout the grid, including chemical and biological variables collected during the sample cruises. Yearly anomalies are calculated by subtracting the climatology from the yearly averages in each grid cell. Further quantification and insight into the interannual variability and its spatial structure is obtained via Principal Components Analysis (PCA). This approach is hindered by gaps in the data in both space

and time (due to weather problems, ship time limitations, etc.) and thus it is necessary to *estimate* a scatter matrix, in this case, the sample covariance matrix, $\hat{\mathbf{C}}$. The sample covariance matrix is obtained from the anomaly time series in the grid, quantifying how the data covary in space and time across the sampled domain. The eigen structure or empirical orthogonal function (EOF) structure is calculated from the sample covariance matrix, representing a physically consistent basis for the observations, where the lower-order EOFs represent spatially coherent structures whose shapes are preserved through time. The time-varying amplitudes of these shapes (the full modal structure of EOFs) are then calculated; these are the principal components (PCs).

3.5.1. Interpolation of the data (optimal analysis)

Spatial data gaps across the grid in particular years are filled, when necessary (e.g., for comparing data fields) using the reduced-space optimal analysis (OA) of Kaplan et al. (1998; hereafter KKCB98). This data-adaptive method produces a smoothly interpolated data set that best preserves the coherent spatio–temporal structure inherent in the data. This is accomplished by: (1) using the eigenvectors from $\hat{\mathbf{C}}$ (described above) as the physically consistent interpolant basis, (2) reducing the space (increasing the signal to noise ratio, S/N) by throwing away those EOFs that represent uncorrelated noise, spatially localized signal or describe little total variance (based initially on classic scree plots, followed by visual inspection of the lowest-order modes being ignored, to make sure they are not valuable in some other respect, though not necessarily describing considerable variance), (3) combining the surviving (dominant) EOFs to provide a smooth, reduced-space interpolant for the data across the grid in space and time, and (4) interpolating the data using an optimal fit of the preserved EOFs to the data for each year (excluding the low-order time-varying constraint used by KKCB98 to prevent abrupt jumps in the interpolated fields from one year to the next, since such jumps *are* apparent in our data).

The advantage of the OA approach is that the interpolant is based on orthogonal functions that describe the natural (observed) covariability across the grid, such that if data are missing for a particular year in a particular grid cell (typically, a single parameter value for the cell), the EOFs take into account how the missing cell value has most consistently covaried with values obtained in other grid cells across the domain. Thus, by optimally fitting the EOFs to existing grid cell data, values in the missing cell are estimated in a manner most consistent with the grid covariability established over numerous other years of observation. The interpolating functions are therefore data-adaptive and not arbitrary mathematical functions.

Domain-shape dependence in the EOF patterns (Buell, 1975, 1979; Richman, 1986) is evaluated by performing tests as described in Martinson and Iannuzzi (2003; hereafter: MI03). The OA allows for estimation of interpolation errors (e.g., the precision with which the EOFs fit a particular year; the accuracy with which missing values are estimated). The sensitivity of all interpolation results are evaluated relative to: (1) grid construction and (2) construction of the scatter matrix (covariance or correlation). The results of the most stable and relevant constructs are presented here.

4. Results

4.1. Maps

Spatial distributions of any quantity are presented on maps. The quantity is interpolated onto a grid that contains the nominal stations and points equidistant between them. The interpolant used for defining the quantity at these grid points is a Gaussian weighted mean. The filtering is necessary in order to make presentation and description of the quantity clear, but is also minimized in order not to eliminate significant features. This interpolated data is then contoured (via lines or colors) onto the maps as presented. Maps include grey lines showing the delimiters of the geographic sub-sections (as in Fig. 1B) as a common reference.

4.2. Primary water mass insights

Examination of the data suggests two fundamental upper-ocean shapes present in T–S space: (1) V-shape, and (2) U-shape (inset T–S plots in Fig. 1). We can imagine a variety of means for maintaining these shapes (involving the strength of WW and overlying ASW), but all have flaws, leaving us still questioning the control. Regardless, the shapes fall into natural geographic groupings of the water masses when presented in terms of the three bathymetric-controlled (slope, shelf and coast of Fig. 1B) sub-regions. The bathymetry seems to serve as a geographic sieve; the sharp V waters dominate the slope waters, whereas the U-shape dominates the coast, and the shelf shows transitional characteristics.

4.3. Relationship to Antarctic Circumpolar Current Waters

A fundamental question concerns the pathways, frequency and distribution of freshly delivered UCDW from the ACC, which supplies heat and nutrients to the WAP continental shelf region. Numerous studies have previously noted the ACC waters sweeping along the slope (as suggested by Sverdrup, 1933; Gordon, 1971a; Orsi et al., 1995; Hofmann et al., 1996, among others). Examination of the historical data (not shown) between 80° and 100°W, at 2° intervals of latitude, suggests that the immediate upstream source for the WAP region is between 68° and 72°S along the Bellingshausen slope. This reflects the ACC waters sweeping to the northeast along the continental slope upstream of the WAP area. A narrow eastwind drift has been documented by Moffat et al. (2008), and labeled the Antarctic Peninsula Coastal Current (APCC).

4.3.1. Water mass tracking.

In the absence of Lagrangian measurements (for which there are very few, in limited regions and years, mainly from SO GLOBEC) water mass tracking is the simplest means for expressing the relationship between the ACC and the WAP grid waters using station data. The most obvious water mass for this is the UCDW, or its modified equivalent on the shelf: M-UCW—in both cases identified as the T_{max} water. While this layer is easily tracked across the grid each year, its distribution is difficult to interpret given the rapid modification of the UCDW by vertical mixing.

Regardless, useful information is apparent when examined in plan view (Fig. 4): (1) warm water is concentrated over the slope in the form of the ACC-core UCDW, (2) warm water is most regularly present in the southwestern extent (over the slope) of the grid, (3) it appears to cool nearly linearly with distance toward the coast in general, (4) there is often a "bulge" of warm water moving onshore along the 300 grid line (northern wall of Marguerite Trough, where the shelf break protrudes into the flow of the ACC likely driving flow into the trough; this is also consistent with the modeling work of Dinniman and Klinck, 2004). These points suggest entry onto the shelf through the canyons cutting across the shelf. Information regarding flushing rates and times are difficult to extract from these data.

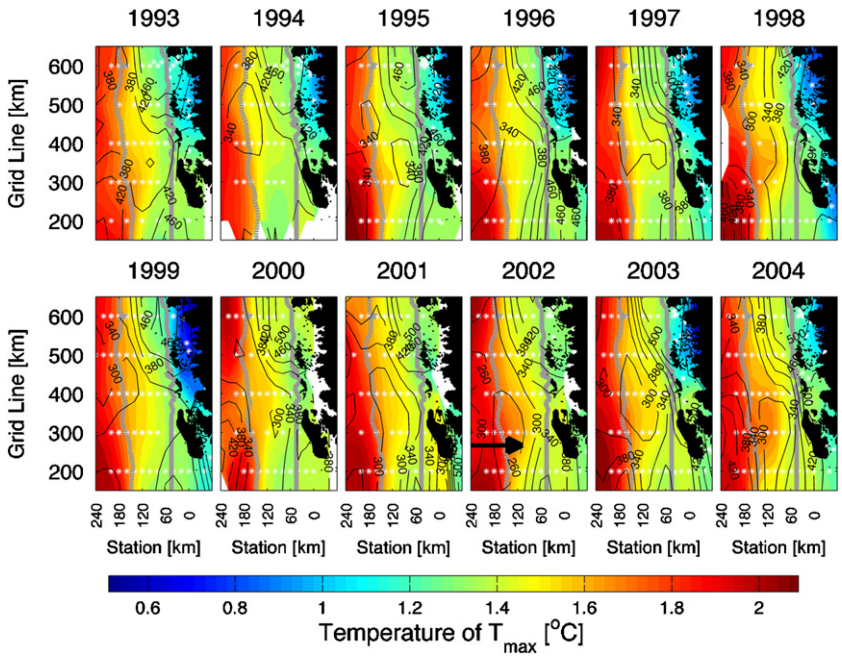

Fig. 4. Colors show temperature of the T_{max} water as it occurs throughout the grid as a function of year; contours show depth of T_{max}. Note "bulge" near 300 line in many years (indicated by arrow in 2002; coinciding with northern wall of Marguerite trough).

The most obvious conclusions drawn from tracking T_{max} are apparent here: the purest UCDW is abundant in the ACC lying over the slope and the 300 line. While the latter is not the only path onto the shelf, T_{max} water appears to regularly show farther inshore incursions there. Short incursions at the 500 line are also common (note from Fig. 1B that there is a canyon at this location as well).

Vertical T-sections as climatologies and annual anomalies (Fig. 5A and B) show incursions of T_{max} water clearly revealing its depth as it moves onto the shelf. Similar sections for salinity (Figs. 5C and D) show that cold anomalies (blue) are usually fresher (blue), and warm (red) ones saltier (red).

4.3.2. Optimal multiparameter (OMP) analysis

While mixing complicates interpretation of M-UCDW across the shelf, OMP strips off one source of that complexity by giving the fraction of pure UCDW at each location, allowing a more direct tracking of the original water mass and its modification. Here we present those results, starting with definition of the defining water properties and water types.

4.3.2.1. OMP water types. Water types and properties defining the *property matrix* **A** for the OMP analysis are chosen as end members in θ–S space, as shown by the labeled rectangles in Fig. 3. The defining properties of these fundamental water types are chosen as follows (summarized in Table 1). For UCDW, we chose pure (regional source) UCDW as it appears in the ACC over the continental slope. Two choices were considered: (1) properties associated with the warmest T_{max} water appearing over the slope (representing the apex of the T–S plot); and (2) the average of the property values of the T_{max} water occurring over the slope. The latter resulted in a considerably reduced error in the OMP fractional occurrence of UCDW (x_{UCDW}), reducing errors in x_{UCDW} between 20% and 38% across the grid per year. Thus, the average characteristics of UCDW over the slope were used.

WW defining properties are determined from the 1999 and 2001 winter stations when WW is in its pure state. DW is defined from deep bottles in 2000–2004, years with good bottle samples in this deep end member. We experimented with using LCDW values sampled off the slope, but this dramatically increased the number of results requiring the nonnegativity constraint, reflecting the fact that LCDW does not occur as an end member water type in our sample grid. As mentioned previously, T is not used as a conservative water property (this exclusion actually improves our fits and their uncertainties, despite decreasing n, supporting our decision that T is nonconservative).

Consistency of the chosen water types is investigated by experimentation (as described above) and through identification and examination of those samples requiring nonnegativity constraints. WW is most frequently in need of these constraints; the consequence of an inadequate water type mixture, most notably reflecting the lack of sea-ice meltwater (and other surface freshwater sources). Initial attempts at including the defining properties of sea ice (e.g., S, N* and Si*) marginally reduced or made no difference regarding this need for constraints, possibly reflecting other surface interactions impacting the WW characteristics. We are still investigating this, but will not comment further on the WW OMP results in this study. Presumably better results could be attained by better sea-ice measurements, which are targeted on upcoming cruises.

DW and UCDW show few regions on the shelf requiring nonnegativity constraints, but the constraints are sometimes required over the slope. Fortunately, the nonnegativity violation of our primary water of interest (UCDW) shows this violation is typically less than 15%, which we consider reasonable given the uncertainties in the fractional values (typically p 20%, though in 1999 was as high as 33%). However, the fact that the constraint is often needed for the same bottle data for UCDW and DW, suggests questionable data quality in those bottle samples over the slope. We are investigating this in more detail, but not here, since the shelf, where the results are best, is the main focus.

A primary focus of the OMP analysis is the distribution and mixing of UCDW as it floods onto the continental shelf from its pure form over the slope in the ACC. For years with data allowing consistent application of the OMP analysis, the maximum fraction of pure UCDW is presented in Fig. 6. Again entry at the mouth of

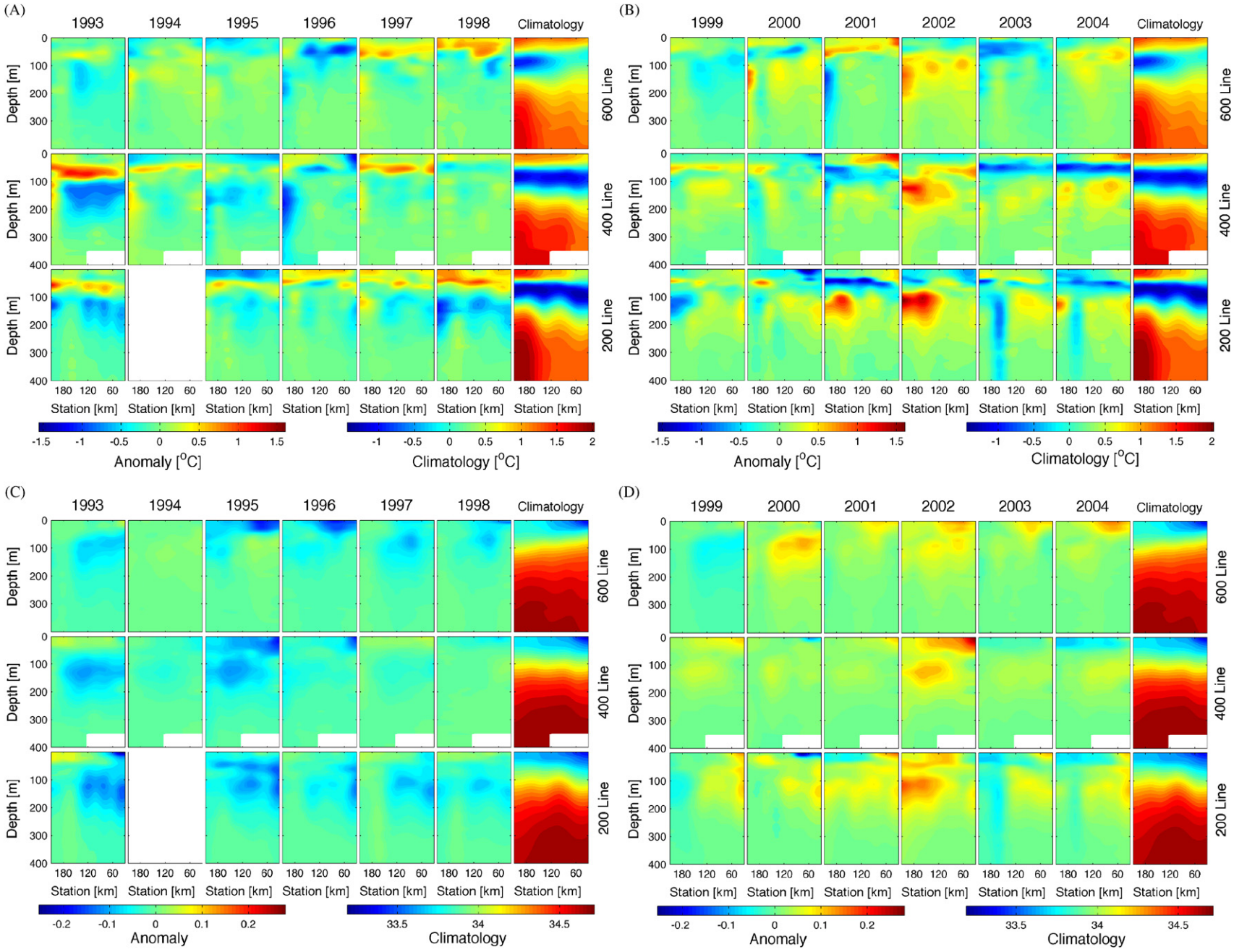

Fig. 5. (A and B) Annual sections of temperature anomalies about their climatologies (right-most column). Anomalies in the upper waters (WW and above) are primarily the consequence of vertical mixing of WW with the surface layer induced by weak (e.g., 1998) or strong (e.g., 2002) winds. Climatologies show WW (blue) and UCDW (red) underlying WW, always over the slope stations, and M-UCDW over the shelf, with greater incursion onto the shelf along the 400 line. (C and D) As above, but for salinity anomalies.

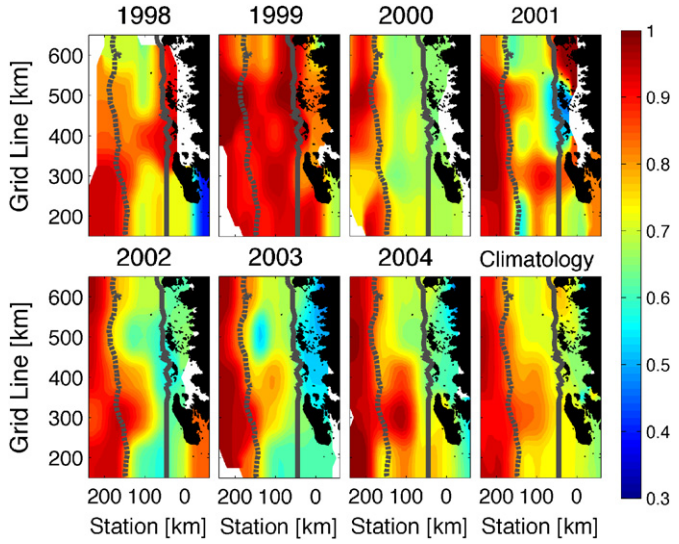

Fig. 6. Annual maps of fraction of pure UCDW (x_{UCDW}) across grid for years in which bottle data were sufficient to allow OMP analysis.

Marguerite Trough (the 300 line) is most apparent, though strong fractions of pure UCDW are seen throughout the grid.

4.4. Geostrophic current structure

Annual geopotential height anomalies (dynamic topography) are computed in the grid within 50–330 m depth for each year of sampling. This allows identification of consistent characteristics of the geostrophic flow field near the base of the surface layer or specific features within it, and relation of UCDW incursions to geostrophy. The geostrophic flow field yields some relatively stable features highlighted by the climatological dynamic topography of Fig. 7A. Two such features are: (1) northward flow along the shelf-break and (2) less obvious, a double-gyre structure on the shelf (previously deduced by Hofmann et al., 1996, from historical data).

Three southern cells are the most consistent features of the multi-gyre structure. The southern cyclonic cell (SC) is present in most years (though its center varies across the shelf). It is usually positioned near the center of the shelf (~100 km offshore (7 40 km) and near the 200 line (7 100 km)). In fact, examination of the surface expression (dynamic topography of Fig. 7A) and deep expression (correlation of depth of deep core, $z(T_{max})$, with dynamic topography, Fig. 7B) suggests that the southern cyclone may be present throughout the southern half of the shelf up to the 450 line (red area in Fig. 7B). That is, the classic cross-section of a cyclone shows a depressed surface (low dynamic topography) mirrored by an elevated deep core. This is precisely the pattern these two figures show, much of the entire shelf center is dominated by a low surface expression (p 1.37 dynamic meters) and this dynamic height depression is precisely that region that shows the strong correlation (12-y time series) of a low dynamic topography with a low (shallow) deep core, faithfully mirroring the surface.

The cyclone is bounded inshore and offshore by what appear to be anticyclones (MA near or over Marguerite Bay, and the OA offshore; neither are fully resolved in space by the sampling). The anticyclones are situated such that their central shelf limbs contribute to the cyclonic circulation. The OA and MA anticyclones appear to be more regular features than the SC itself. In fact, the OA appears in every January for the entire 12 years of these data, but its presence may simply reflect the influence of topography on the ACC since the ACC has increasing geopotential height farther offshore. There is also a tendency for the isodyns to turn offshore at a bend of the shelf break (between the 200 and 300 lines) south of which the OA is often centered. Interpretation of the MA cell is complicated by examination of the dynamic topography on a yearly basis, and the fact that the current field analyses from SO GLOBEC indicate a cyclonic circulation cell in Marguerite Bay (Beardsley et al., 2004; Klinck et al., 2004).

Two dynamic topography characteristics are of particular interest: (1) The central portion of the grid most consistently shows the tendency for cross-shelf geostrophic flow, usually from the slope toward the coast, consistent with the cyclone, though this is sometimes reversed, (2) in 2002 in conjunction with the largest incursion of UCDW onto the shelf at the 300 line (Figs. 6 and 7C), the OA is least well developed, and the SC is particularly strong—consistent with the shallower location of the UCDW in that incursion.

4.5. Sensible heat flux

4.5.1. Bulk property estimates

4.5.1.1. Vertical diffusivity coefficient, k_z. The bulk property methodology of MI98, requires an optimal estimate of the turbulent vertical diffusivity coefficient, k_z, here based on the warming of a layer H_{WW} of trapped WW at each station. Optimal values of k_z over the shelf averages ~$8.5 \times 10^{-5}\,m^2\,s^{-1}$, versus the p 1×10^{-5} average value estimated from microstructure in the southern part of the grid by Howard et al. (2004), 0.66×10^{-4} for the central Weddell gyre (Martinson, 1990), 7×10^{-4} from Smith and Klinck (2002) via modeling, and 7.7×10^{-4} from Klinck et al. (2004). The latter is that value required to balance their estimated advective rate of UCDW flooding of the shelf. The role of double diffusion is still unresolved (e.g., Howard et al., 2004), and not dealt with here.

4.5.1.2. Bulk property diffusive heat flux. The diffusive heat flux and total annual ocean heat flux change dramatically depending on whether we use a single multi-year optimal value of k_z for all years (a typical approach in most modeling studies) or the annual optimal value for each individual year. With a single multi-year value, the total annual ocean heat flux shows a steady increase throughout the LTER sampling period (0.17 0.001 $W\,m^{-2}\,y^{-1}$) and a strong linear relationship ($r^2 = 0.84$) with the heat content on the shelf (Q_{shelf}). Q_{slope} shows a strong linear relationship with Q_{shelf} ($r^2 = 0.77$), allowing us to examine the historical Q_{slope} data as a proxy for ocean heat flux on the shelf (contributing to atmospheric warming).

However, the optimally calculated value of k_z decreases steadily through our sampling period (Fig. 8) and we have chosen to use this varying k_z (the optimal value for each individual year), as being most representative of F_{DT}. For this, the diffusive flux decreases with k_z, negating the increasing trend in annual heat flux, eliminating any correlation with the increasing Q_{shelf}.

Using the optimal k_z for each year and the Large and Yaeger (2004) $\bar{F}_{air}$ (32.5 $W\,m^{-2}$) for all years, the climatological winter-average ocean diffusive heat flux averages / $F_{DT}S_{BP\text{-}shelf}$ = 8.67 2.6 $W\,m^{-2}$, with the largest values in the northern extent of the grid decreasing diagonally across the grid toward the mouth of Marguerite Bay.

4.5.1.3. Entrainment heat flux. The multi-annual average entrainment heat flux on the shelf, $\langle F_{ET}\rangle_{BP\text{-}shelf} = (TB_w\text{=}R)(\bar{F}_{air} - F_{DT}) = 18{:}7 \pm 2{:}1\ W\,m^{-2}$.

4.5.1.4. Annual heat flux. F_{DT} and F_{ET} are combined to give the annual average ocean heat flux / $F_{ann}S$. Its climatology is

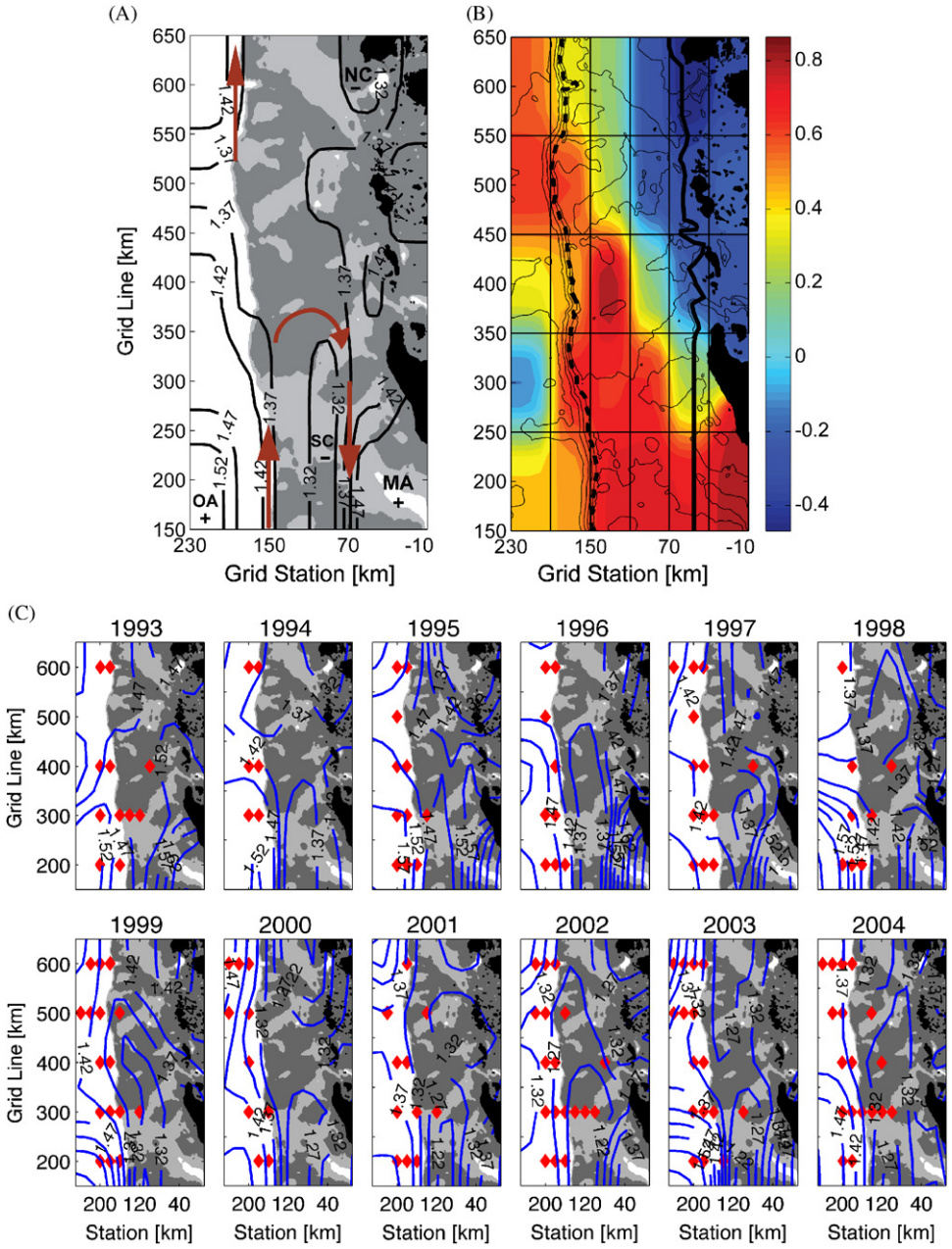

Fig. 7. (A) Dynamic topography (50–330 db) climatology, with stable features noted (OA: offshore anticyclone; SC: shelf cyclone; MA: Marguerite Bay anticyclone; NC: northern cyclone), arrows show primary geostrophic flow directions. (B) Correlation map between dynamic topography and depth of T_{max}, showing that depth of UCDW is regulated in general by dynamics (color bar shows *r*-value). (C) Annual maps of dynamic topography (blue color contours); grey-scale topography as in Fig. 1B; light gray areas are canyons in the shelf), red triangles show locations with pure UCDW present.

shown in Fig. 9A; the multiyear annual average over the shelf, / $F_{ann}S_{BP\text{-}shelf} = 15.67\ 2.8\,W\,m^{-2}$. The spatial distribution of trends in F_{ann} (Fig. 9B) shows decreasing trends over most of the grid, with increasing trends over the SW slope. On average, the shelf heat flux / $F_{ann}S_{BP\text{-}shelf}$ shows considerable variability. Fitted with a trend yields a weak decreasing trend over the sampling years (Fig. 9C) of $-0.597\ 0.58\,W\,m^{-2}\,y^{-1}$.

PCA of the F_{ann} anomalies (Fig. 9D) reveals that the dominant mode of variability, describing over 57% of the total variance, temporally undergoes an exponential decay with interannual cycling superimposed. Year 1997 appears as a strong peak in the PCs of the first three modes (describing a total of ~77% of the total temporal variance).

4.5.2. Ocean heat content estimates

F_{ann}, estimated via inversion using $DQ^{total\,Q}_{shelf}$, yields a 12-year average of: / $F_{ann}S_{Q\text{-}shelf} = 16.5\,W\,m^{-2}$, but the diffusive and entrainment values are unreasonable (giving a small negative diffusive value). The comparable estimate from the bulk property method is / $F_{ann}S_{BP\text{-}shelf} = 18.67\ 3.4\,W\,m^{-2}$. Interestingly, $DQ^{total\,Q}_{shelf}$ for the southern half of the shelf where the southern cyclone (SC) is always present, / $F_{DT}S_{Q\text{-}SC} = 13.8$, / $F_{ET}S_{Q\text{-}SC} = 9.4\,W\,m^{-2}$, / $F_{ann}S_{Q\text{-}SC} = 18.1\,W\,m^{-2}$ and / $F_{DT}S_{BP\text{-}SC} = 9.4$, / $F_{ET}S_{BP\text{-}SC} = 17.6\,W\,m^{-2}$ / $F_{ann}S_{BP\text{-}SC} = 21.67\ 3.5\,W\,m^{-2}$. In each case, the annual heat flux estimates agree to better than 20% with the *Q*-based estimate consistently higher than the bulk property estimate. In the simplest sense, the 20% inflation could be ascribed

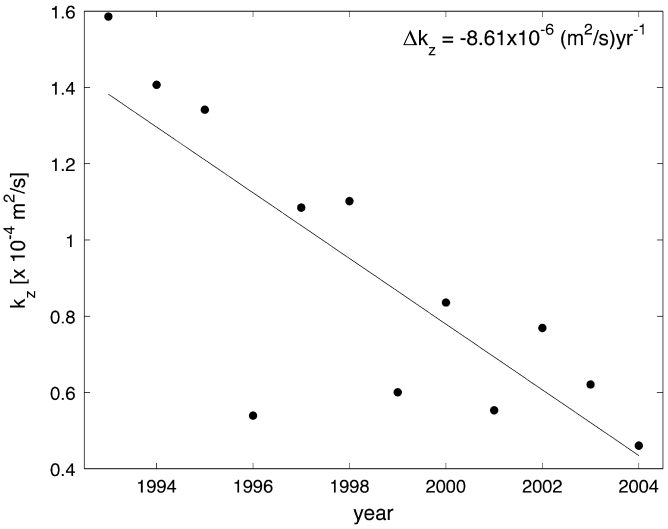

Fig. 8. Change in shelf-average k_z as function of time, with least squares fit trend line. Annual trend is given as inset.

to an average of 1.2 full-flooding events of the SC per year, or, likewise, there was one full-flooding event with leakage from Marguerite Trough over the years accounting for an equivalent of 20% of this SC area. However, as previously stated this $DQ_{shelf}^{total\ Q}$ contains changes in Q attributed to direct mixing of water masses, also inflating it, something that could account for the discrepancy without any alteration to the one full-flooding event per year. Results from this heat content approach is encouraging and clearly warrants more detailed consideration.

4.5.2.1. Change in heat content with time. One clear indication of the history of the heat supply to the continental shelf waters is apparent in the change in Q_{shelf} as a function of time (Fig. 10A). Q_{shelf} shows a steady increase with time over the 12-year period of this study, amounting to a change of $\sim 2.56 \times 10^7\,J\,m^{-2}\,y^{-1}$ with r^2E 50%. There are not sufficient historical shelf data to extend this calculation back in time, but historical data are available over the slope (NODC and Southern Ocean Atlas; Orsi and Whitworth III, 2005). Q_{slope} is linearly related to Q_{shelf} ($r^2 = 0.77$), establishing Q_{slope} as a proxy for Q_{shelf}. As seen in Fig. 10B, decadal averages of Q_{slope} are variable in years preceding LTER sampling; except for a single station in 1956, the pre-1990 (o 1990) decadal average values are considerably lower than the LTER (X 1990) decadal averages: / $Q_{X\ 1990}$S = (3.837 0.07) × 10^9; versus / $Q_{o\ 1990}$S = (2.987 0.16) × 10^9, uncertainties given as one standard error in the mean. The likelihood of these two means being equal is negligible (o 0.01).

This jump in available heat content from the end of the 1980s until the 1990s is comparable to warming the entire 300-m sub-WW layer on the shelf by ~0.7 1C. For this analysis, the pre-LTER Q_{slope} values are integrals of existing slope stations, which varies from year to year (the number of stations going into the average values are indicated on the plot, inside abscissa). The source of the tremendous increase in shelf heat content is investigated in Section 5.

4.6. Other bulk properties

4.6.1. Climatologies and spatial distributions

Eventually, we wish to establish covariability between various physical variables, and between physical and ecological variables. One obvious starting point is examining climatological distributions, here starting with the three fundamental bulk properties (SD_w, TB_w and R, Fig. 11). An interesting feature is the apparent disconnect between SD_w and the spatial patterns of the other two variables. For SD_w, Marguerite Bay seems to exert a strong influence on the salinity controlling SD_w, a pattern often seen in other physical variables across the grid (e.g., SD_s and z_{wm}). The similarity between TB_w and R reflects the dominance of TB_w on R.

As a test of the method to estimate winter bulk property values from summer profiles, we compared R estimates produced from summers with subsequent winter profiles from the same locations (3 years); the summer estimates agree with the winter estimates at better than 83%. Also, as required for the bulk property methodology, lateral property gradients are relatively small (e.g., T_{max} shows the largest lateral gradient across the shelf break, with climatological gradients peaking in the southern extent of the grid at $\sim 5 \times 10^{-3}$ 1C km^{-1}; a trivial change in the direction of minimal current flow). Given that the interannual variability about the climatology is small, this small lateral property gradient satisfies a primary condition for application of the bulk property distributions. Similarly, in the Weddell Gyre, MI98 were able to use the method along the northern rim of the gyre, which was bounded by the ACC, but again, the largest gradients were perpendicular to the stream.

4.6.2. Interannual variability

SD_w shows anomalies distributed rather evenly across the grid, but dominated by a notable full-grid drop (more freshwater in the upper layer) starting in 1998 (Fig. 12). As seen in its yearly anomalies, there is a major shift from positive anomalies (equivalent to ~0.25 m of sea-ice thickness additional freshwater) through 1997 to large negative anomalies (also ~0.25 m thickness equivalent) starting in 1998. The dramatic shift is also apparent in SD_s (not shown) appearing in the January 1999 data (whereas it appears in the winter of 1998 as calculated for SD_w).

The other bulk properties show similar anomalies but none of them appear to be particularly noteworthy so are not shown (see http://www.ldeo.columbia.edu/~dgm/MartinsonLTERDSR). There is indeed a shift in TB_w comparable to that in SD_w though it is not visually as apparent because of the signal to noise ratio of TB_w; R mimics TB_w though the inclusion of SD_w in this parameter makes the shift more apparent.

4.7. Near-surface ocean interannual anomalies

Vertically averaged anomalies, T' and S' (relative to the 12-year station climatologies) are generated for each year at each station, integrated above the WW (T_{min} water), giving the vertically averaged anomaly of the summer surface water, and likewise below the WW, giving the vertically averaged circumpolar water anomalies. As seen in the near-surface S' for the 600 line (Fig. 13), there appears to be an increase in the salinity anomalies (towards more salt) with time (consistent with the deeper wintertime SD_w anomalies of Fig. 12).

Surface ocean temperature anomalies (T') show similar lateral property gradients when moving from the slope toward the coast; the property gradients are comparable for each year (suggesting the mixing of two end-member water masses) resulting in a constant T:S of ~2:1 (1994 and 1996 show T, but not S gradients).

5. Discussion

5.1. Discussion

5.1.1. Water masses

Water-mass analyses and distributions corroborate results seen or assumed in previous studies (as referenced in text): the

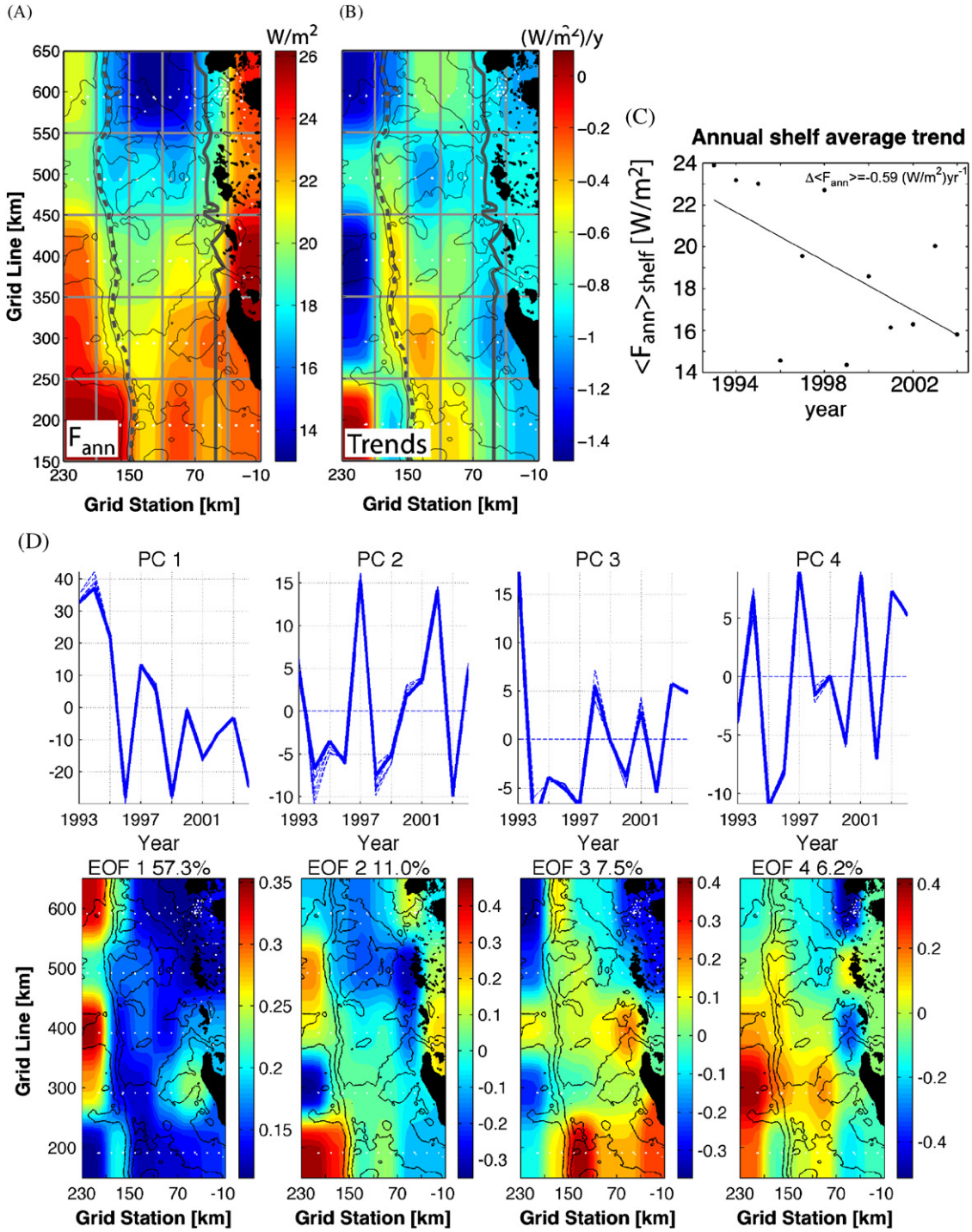

Fig. 9. (A) Annual-average ocean heat flux F_{ann} ($W\,m^{-2}$). (B) 12-year trends in F_{ann} ($W\,m^{-2}\,y^{-1}$). (C) Change in annually average shelf-wide F_{ann} as function of time, with LS fit shown. (D) First 4 modes of F_{ann}. Presented as principal component (time expansion coefficients, upper panels) over their spatial pattern (lower panel). Fraction of described temporal variance shown between upper and lower panels. Gravest (dominant) mode shows exponential decay with interannual cycle superimposed evenly distributed across entire grid.

WAP continental shelf is flooded by UCDW. The proximity of the UCDW to the continental shelf is steady throughout the 12 years—it always lies over the slope, showing the southern limit of the ACC consistently bounded by the shelf-slope break; subtle variations (of unknown time scale) occur when flooding events show on-shelf incursions.

Several details are apparent from tracking T_{max} and examining water-mass fractional compositions (OMP analysis): the purest UCDW is abundant in the ACC lying over the slope. The farthest incursions onto the shelf appear to coincide with the location of Marguerite Trough at the 300 line; short incursions at the 500 line are also common (note from Fig. 1B that there is a canyon at this location as well).

OMP results show clear interannual variability in the distribution of the fraction of pure UCDW across the shelf. The 7-year climatology in Fig. 6 shows that the 300 line most consistently shows the highest fraction of pure UCDW. The spacing of the station lines does not allow us to distinguish the long-shelf width

of incursions to better than the 100 km grid line spacing. But in years when a high fraction of UCDW is *only* seen coming in on the 300 line (e.g., 2001 in Fig. 6), it is not seen at the bounding grid lines implying that the water may indeed be entering only within the trough. Klinck et al. (2004), using SO GLOBEC current meter data, explicitly document this inflow via Marguerite Trough.

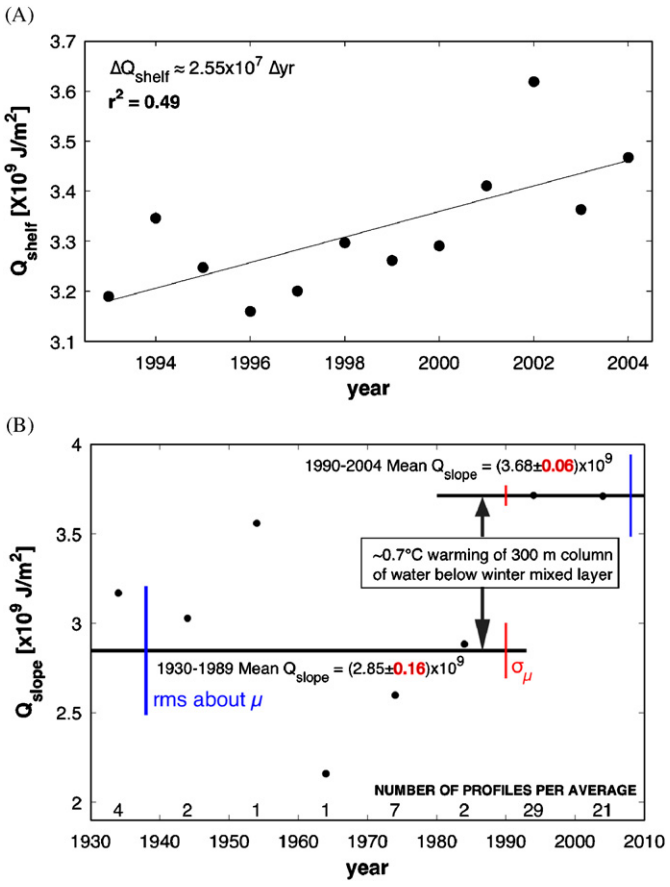

Fig. 10. (A) Heat content on shelf (Q_{shelf}) as a function of time. (B) Decadal averages of Q_{slope} as function of time, with average Q_{slope} values for period before LTER and during LTER showing tremendous jump in slope heat content.

5.1.2. Ocean heat

Probably the most striking result is the increasing ocean heat content over the continental shelf, likely reflecting the influence of one or more of these three mechanisms: (1) no change in source water and its flooding of the shelf with a reduced heat flux to the atmosphere venting the supplied ocean heat more slowly, (2) more UCDW is upwelled onto the shelf from the slope, and/or (3) warmer water being delivered to the WAP by the ACC (i.e., UCDW is warming). All three appear to be clear contributors.

The first mechanism likely contributes since F_{ann} shows a poorly-fit decreasing trend. So, unless the supply of heat to the shelf is reduced commensurately (via mechanism 2 and/or 3), the reduction in F_{ann} in time must lead to an increase in Q_{shelf}. How much this contributes is a function of the role of the other two mechanisms.

The second mechanism (increased supply of UCDW to the shelf) could be due to increased upwelling over the shelf, and/or more frequent flooding events (though wider shelf coverage of the flooding events likely equates to increased upwelling). We do not have evidence to address the latter, but the former is evaluated by examining the covariability of Q_{shelf} to a practical index of upwelling: here the thickness of the pycnocline (being thinner when upwelling is stronger). As shown in Fig. 14A, this relationship is strong ($r^2 = 0.84$), so more warm water is being pulled onto the shelf as evidenced by a thicker layer of warm water (i.e. sub-WW water).

Finally, the third mechanism is investigated through the covariability of Q_{shelf} to T_{max} over the slope (Fig. 14B). For the well-sampled LTER years, there is a clear but weak relationship, suggesting a small fraction (~21%) of the shelf warming during the 12 years of sampling can be attributed to more heat (as warmer UCDW) delivered to the region over this time period. This warmth is illustrated by a 0.011 °C y^{-1} increase in T_{max} on the shelf ($r^2 = 0.87$).

However, on longer time scales, the remarkable jump from the pre-1990 average to the 4 1990 average (of Fig. 14B) suggests that this supply *has* increased, and in fact, dramatically so over the period of the strongest AP warming. This result is consistent with numerous studies uncovering signs of ocean warming (e.g., Fahrbach et al., 1998 and Robertson et al., 2002 in the WDW of the Weddell Sea; Gille, 2002 in the Southern Ocean; Barnett et al., 2001 in the global oceans; Meredith and King, 2005 in Marguerite Bay surface waters), though how those relate mechanistically to the warming noted here, if at all, is yet to be determined.

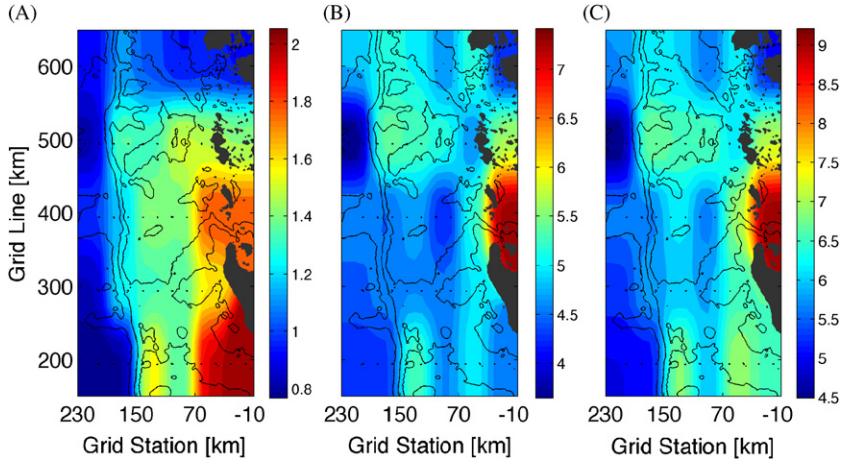

Fig. 11. Twelve-year climatologies of primary bulk parameters: (A) winter salt deficit (m), SD_w; (B) thermal barrier (m), TB_w; and bulk stability (m), (C) R. The radiating rectangular pattern in the lower right of (A) reflects a pattern often observed in property distributions, with anomalous values in Marguerite Bay.

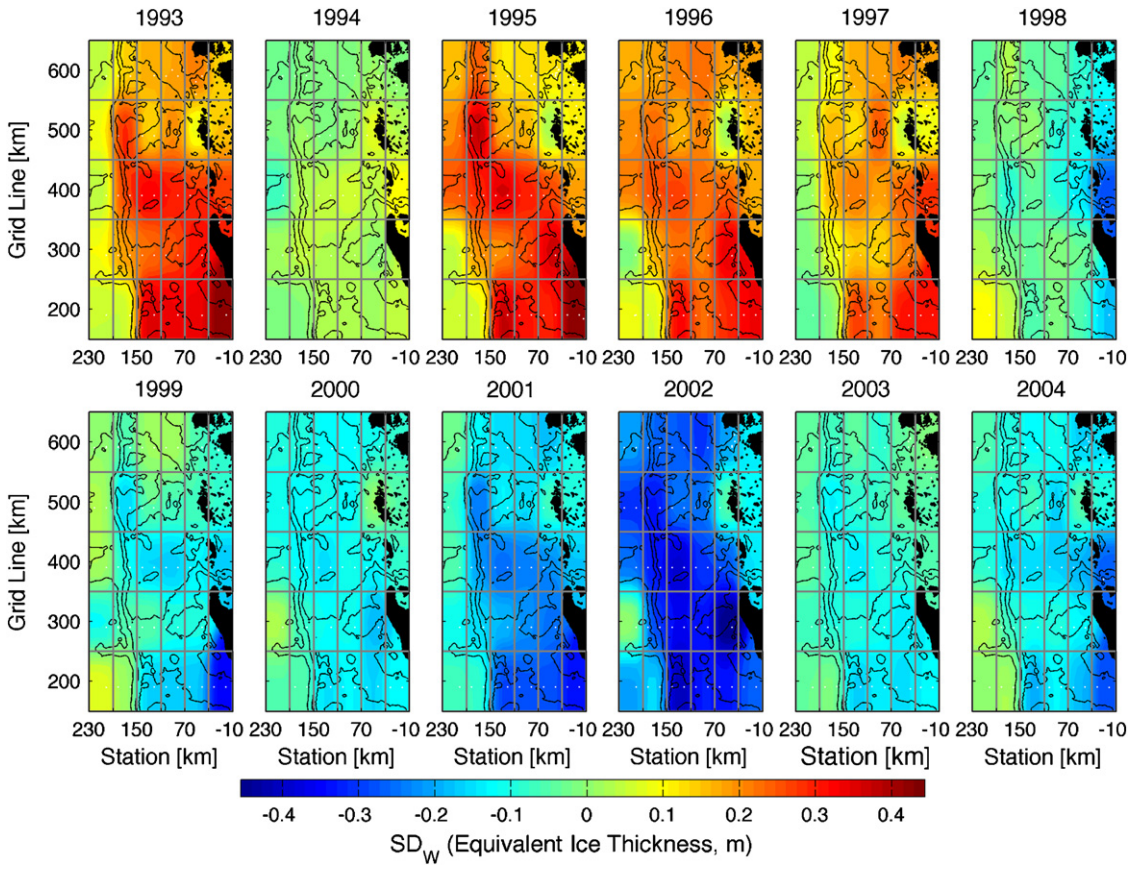

Fig. 12. Annual optimally interpolated anomalies in winter salt deficit about 12-year climatology. Note large jump in anomalies from primarily positive across the grid through 1997, to primarily negative (less freshwater in winter mixed layer) since 1998. Color bar shows equivalent sea-ice thickness in m.

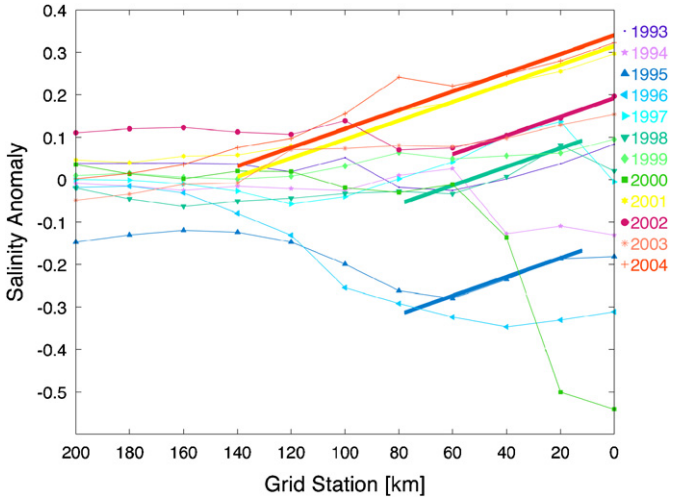

Fig. 13. Vertically integrated summer surface (above WW) salinity anomalies (about the 12-year climatology) at each station on the 600 line for each year. Note that the 2002 anomaly starts at a higher value than all others, consistent with the unusually large UCDW incursion during that year (and unusually positive, saltier, anomaly in SD_w, Fig. 11). Years 1995 and 2000 freshen toward the coast, with 2000 being particularly dramatic.

The ocean heat flux, F_{ann} is a sensible (cooling) heat flux. The flux to the winter atmosphere from the surface (F_{air}) is a combination of sensible and latent heat (ice formation) fluxes while that flux through the ocean to the surface is strictly sensible, so $F_{air} \neq F_T$ (though experience suggests that they are often nearly in balance by mid-winter). The latent heat flux is released to the atmosphere in winter during times of freezing, but returned upon melt; it is not clear if this seasonal redistribution of heat plays any significant role in the winter regional warming. The sensible heat provides a net contribution to the region from afar, courtesy of the global thermohaline circulation.

On the shelf, the ocean heat is passed from the water to the atmosphere through leads and other openings or to the underside of sea ice, melting it. Therefore, the increased availability of heat on the shelf is likely playing a role in the recently observed increase in the strong atmospheric warming and marine glacier melting on the western side of the Antarctic Peninsula (Cook et al., 2005), decreased sea ice concentration (Liu et al., 2004), and decreased length of sea-ice season (Parkinson, 2004; Stammerjohn et al., 2008a).

5.1.3. *Bulk properties*

The winter salt deficit (SD_w) is a measure of the upper-ocean freshwater content contained within the *winter* mixed layer and permanent halocline that overlies the saltier deep water below the permanent pycnocline (Fig. 3). The shift from positive to negative anomalies in 1998 (Fig. 12) is equivalent to eliminating nearly 0.5 m of sea-ice melt (the dominant source of surface freshwater away from the coast). This freshwater is no longer mixed into the winter mixed layer between 1998 and 2004, suggesting a net loss in freshwater throughout the winter mixed layer. This increased salinity is consistent with Meredith and King (2005) who note significant trends towards increased summer surface salinities off of the WAP, which they relate to decreasing winter-sea ice extent.

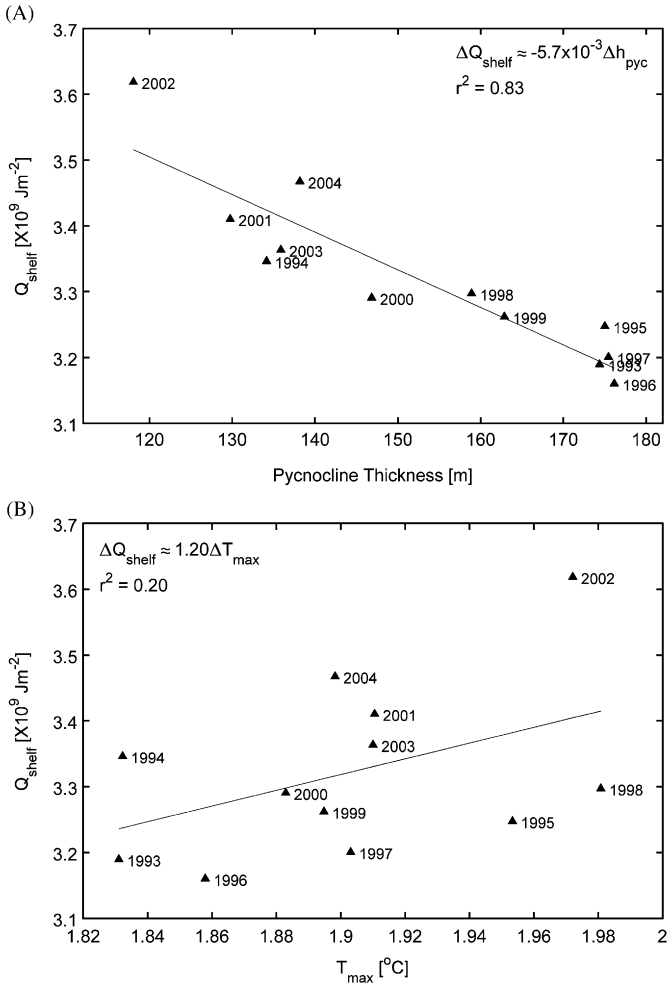

Fig. 14. (A) Relationship of heat content on the shelf (Q_{shelf}) to upwelling, as indicated here by thickness of permanent pycnocline (thinner pycnocline results from stronger upwelling). (B) Relationship between Q_{shelf} and temperature of T_{max} water (UCDW) over slope (warmer UCDW results in more heat on shelf due to delivery of warmer water).

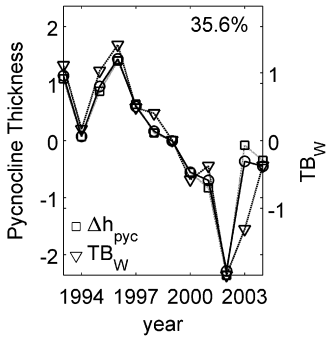

Fig. 15. Leading mode PC of TB_w (triangles), permanent pycnocline thickness (*x*'s) and coupled mode (circles). The coupled mode accounts for nearly 36% of the total temporal covariance between these two variables.

As discussed previously, SD_s, away from the coast, is a strong indicator of the *previous* winter's sea-ice cover thickness. The shift in the January 1999 SD_s indicates there was a shift towards less sea ice in the winter of 1998 (confirmed by Stammerjohn et al., 2008b), coincident with a shift towards a saltier winter mixed layer as indicated by the 1998 shift in winter salt deficit discussed above.

This shift in the winter bulk properties in 1998, coincident with sea-ice changes, and subsequent summer bulk properties in January 1999, all indicate that a fundamental change occurred in the waters of the WAP in 1998. The most likely contributor to this shift is the UCDW, which is intruding at shallower depths, bringing in anomalous heat (Figs. 5A and B, 9, and 10) and salt (Figs. 5C and D, and 12). The seemingly counter-intuitive *reduction* in TB_w in 1998 reflects a compaction of the thermocline associated with the enhanced upwelling of UCDW to shallower depths (Fig. 15).

The role of UCDW is also apparent by the correlation of the permanent pycnocline thickness and Q_{shelf} (Fig. 14A). About 60% of the pycnocline thickness change is due to changes in the depth of the it base; the UCDW is lifted closer to the surface, yet the surface conditions are not changing as much, so that the top of the permanent thermocline remains similar while its base is raised to shallower levels. This decreases the net heat content of the upper waters (as measured by TB_w), while filling the sub-thermocline waters with warmer UCDW (in place of transitional thermocline water), thus increasing Q_{shelf}, as shown in Fig. 10A. So, this increased upwelling of UCDW yields increased deeper heat content and less upper ocean (thermocline) heat content. It may also explain the reduction in k_z, since simple bulk parameterizations of k_z as a function of Richardson number are extremely nonlinear (e.g., Pacanowski and Philander, 1981; Mellor and Yamada, 1982), and consistent with lowering k_z with increasing stratification expected with the compression of the pycnocline, so this may also explain the reduction in k_z, which leads to the reduction in F_{DT} and F_{ann}.

Bulk stability shows a climatological spatial pattern (Fig. 11C) that reflects the controlling TB_w (TB_w controls 70–85% of the value of R). That adds tremendous effective stability to an otherwise weak static stability across the permanent pycnocline. It is remarkable that this weak stability can resist overturn, but the resistance is afforded by the tremendous heat content of the pycnocline (that dominates R); even the smallest amount of sea-ice growth leads to the release of a tremendous amount of pycnocline heat via the entrainment heat flux, which melts ice and stabilizes the water column more. Bulk stability values show that typically between 6.5 and 7.0 m of *in situ* sea-ice growth would have to grow *in situ* in order to overturn the water column and induce convection (and bottom water formation); the likelihood of this is discussed below.

Finally, some features in the bulk property climatologies worth noting:

(1) Visually striking in Fig. 11B and C are the anomalously strong values of TB_w and R behind Lavoisier Island (this is at the northern end of an inland passage, "The Gullet", connecting this area to Marguerite Bay behind Adelaide Island). One might naturally attribute this to intense freshening by glacial melt runoff, but this is not the case. While the surface water in this location is indeed very fresh and cold (likely glacial runoff), the T_{min} layer is actually a bit warmer and T_{max} a bit cooler, leading to a weaker $\nabla_p T$ and thus a deeper integration limit for TB_w. As previously stated, TB_w dominates R, and it is exceptionally so here, leading to an incredible 9 m of R. It is not clear what role the Gullet plays and exchange with Marguerite Bay plays in this feature, but there is clear exchange through the Gullet, as evidenced by one of the Beardsley drifters, which in April 2006, passed through the Gullet into Marguerite Bay from the north (see http://www.whoi.edu/science/PO/LTER_Drifter/index.html). Later drifters in the same array reached the northern end of the gullet, but instead of passing through, turned around and flowed around Adelaide Island to the north and west. Whether that reflected

a reversal of the Gullet flow or unfavorable winds, is not clear.

(2) Property distributions like that of SD_w (Fig. 11A) highlights the strong contrast in values coming out of Marguerite Bay as well as high values behind Lavoisier Island (at the coast inside of the 400 grid line). This distribution also displays an on-to-offshore gradient in the lower two-thirds of the grid, common in some biogeochemical variables, and a cross-shelf pattern in the upper portion of the grid.

(3) At the southwestern shelf break, between the 200 and 300 lines, the summer surface freshwater content (indicated by SD_s) is substantially less than the amount of sea-ice melting *in situ* (one of 2 locations in the grid where the number of days covered by ice is not well correlated to SD_s, see Fig. 7 in Stammerjohn et al., 2008b) implying that the higher salinity UCDW is consistently intruding into the surface waters in this region, thus increasing its salt content (or decreasing its freshwater content)—further evidence of UCDW influence consistent with dynamic topography.

5.1.4. Surface property gradients

The lateral surface gradients (S' and T') are consistent with linear mixing that is proportional to the distance from the slope (i.e., incursions of UCDW toward the coast), such that the closer to the coast the incursion, the stronger the anomaly (coastal regions are least influenced by the UCDW, so when it does approach, it causes a large jump in properties relative to climatology). A 2-variable linear regression suggests that a large fraction of the multi-year average salinity anomalies (~96%) are described by the relationship of distance of incursion from slope, and 34% of the residuals about that regression are *fit* by regressing the residual salinity anomaly against surface air temperature (reflecting a sea-ice impact in addition to the UCDW mixing effect); this relationship is particularly strong in the middle of our 500 line, about 100 km south of Palmer Station; elsewhere it is weaker, so the relationship is not clear enough to claim a good understanding of the underlying mechanism responsible for these observed relationships.

Summer surface anomalies may seem counterintuitive (increasing S' coastward; we anticipated an increased freshening with time toward the coast as glacial meltwater input increases), but the 34% residual relationship of the S' to SAT, hints that the warming is also leading to a decrease in sea-ice production in the coastal region, and therefore, the 34% reflects that contribution of the sea-ice meltwater dominates that of glacial meltwater.

5.1.5. Regional climate forcing

The WAP is in the heart of the region, the Antarctic Dipole (ADP), showing Earth's largest extratropical surface response to ENSO events (Yuan, 2004). Rind et al. (2001) show that El Niño events favor the subtropical jet over the polar jet in the Pacific sector, leading to a reduction of polar lows impacting the WAP. The opposite is true of La Niña, which has been shown to provide a more consistent forcing with strong polar low forcing (note that the Weddell side shows the opposite response as the Pacific side). Yuan (2004) nicely summarizes all of these responses for both positive (El Niño) and negative (La Niña) ENSO events. WAP climate is also influenced by the state of the Southern Annual Mode (SAM). A positive bias in SAM leads to a WAP response similar to that of La Niña (Stammerjohn et al., 2008a).

As suggested by Stammerjohn et al. (2008a), the rapid atmospheric warming in the AP region during autumn and winter may be driven, in part, by changes occurring in the atmospheric circulation during austral spring, summer and autumn. These atmospheric circulation changes include stronger and more frequent northerly winds over and to the west of the AP region, which are in turn associated with moderately earlier spring sea ice retreats but significantly later autumn sea ice advances. Thus, the summer ice-free season is becoming longer and the winter sea-ice season shorter. These ice-atmosphere changes would amplify the increase of air temperature in autumn and early winter given the stronger trend towards a later autumn sea-ice advance (sometimes well into July), changes that would be accompanied by dramatic increases in air–sea heat fluxes as day-length decreases into autumn (but not accounted for here through the use of a single F_{air}, reflecting a need for measurements of the surface energy balance).

The reduced impacts on sea ice in the AP region occur in response to La Niña and/or positive SAM. While the high-latitude response to La Niñas have become stronger in the 1990s, the SAM has become more positive in the 1990s (e.g., Thompson et al., 2000; Marshall, 2003), especially during late spring to early autumn, and it has been suggested that SAM may be amplifying the high-latitude response to ENSO events in general (Fogt and Bromwich, 2006; L'Heureux and Thompson, 2006) though La Niña events in particular (Stammerjohn et al., 2008a). In short, not only does a positive bias in SAM impact atmospheric warming directly (e.g., Thompson and Solomon, 2002), it also causes changes in circulation that likely contributes to increased UCDW intrusions (Stammerjohn et al., 2008a) and shorter sea-ice seasons (most noticeable between 1980s and 1990s), both of which positively feedback on each other, thus amplifying regional AP atmospheric warming from shelf waters. Venting of UCDW heat in the coastal region is likely contributing to the atmospheric warming as well as the glacial melting.

It is not clear how the frequency of flooding has changed, but we do know that the winds vary with the large-scale climate patterns that influence the region (e.g., Liu et al., 2004; Lefebvre et al., 2004) and they have undergone large variability in recent years, thus would likely impact the frequency of flooding events.

5.1.6. Currents

Klinck et al. (2004), using SO GLOBEC ship-based ADCP and Beardsley et al. (2004) drifter data in the southern portion of the grid, noted cyclonic circulation in Marguerite Bay. They found that cell to be ephemeral (mostly in winter), and that the dynamic topography did a good job of indicating direction, but only resolved ~50% of the actual current speed. Our 12-year climatological isodyns are often curved so as to hint at the presence of an anticyclone in Marguerite Bay (MA on Fig. 7A), but our dynamic topography is for 50–330 m, giving a view of the geostrophic flow at the base of the surface layer, whereas Klinck et al. (2004) are for the surface to 400 m. Thus, the difference may represent a shallow cyclone, perhaps in response to the freshwater surface outflow from the coast, underlain by a deeper opposite spinning anticyclone. Alternatively, our anticyclone may be an erroneous extrapolation based upon our partial view of only the western most limb of the MA cell. The isodyns in this limb do not always turn so as to *appear* to make a closed cell in Marguerite Bay; in many years the isodyns continue parallel to the shelf break, with increased dynamic height into the bay, which may imply that the SC is expanding into the bay as a *cyclone*. This is not clear, but will not be investigated further, given our limited velocity information.

The depth of T_{max} is well correlated to the dynamic topography throughout most of the grid (Fig. 7B), except for the northeastern coastal region (the blue colors in Fig. 7B). This suggests that the more consistent geostrophic features on the shelf SW of the 450-km grid line, relative to the more irregular nature of those in the northeast, play an important role in the UCDW flow onto the shelf. Uplift of the isohalines (enhanced upwelling) in the center

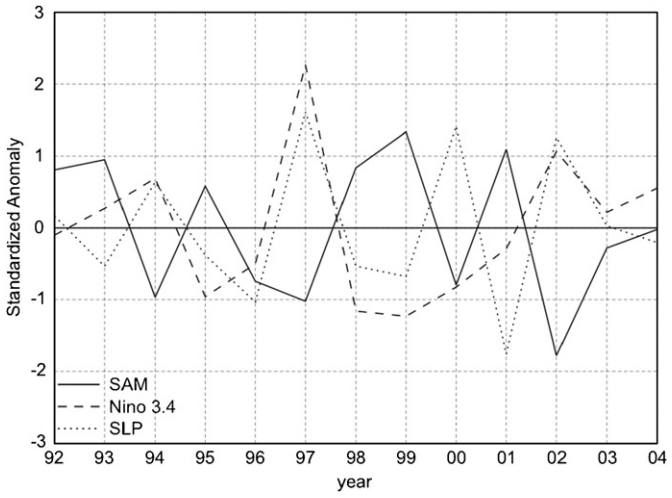

Fig. 16. Time series of September–October–November averages of SLP (solid), Niño 3.4 (dotted) and SAM (dashed). The SLP are from a location centered on 651S, 901W and are numerically analyzed data from the National Center of Environmental Prediction and National Center for Atmospheric Research Reanalysis (NNR) Project (Kalnay et al., 1996). The ENSO index is the Niño 3.4 sea-surface temperature index consisting of averaged eastern equatorial Pacific sea-surface temperature for 51N–51S, 170–1201W (Cane et al., 1986; available at http://iridl.ldeo.columbia.edu/). The SAM index used here is an observation-based index provided by *Gareth Marshall* (available at http://www.nerc-bas.ac.uk/icd/gjma/sam.html) (Marshall, 2003).

of the cyclones is particularly evident in years when the cyclones are stronger than usual, suggesting surface divergence and deep water inflow onto the shelf (see below). Thus we conclude that the UCDW is pulled onto the shelf during periods of cyclonic forcing, strongest in the southern half of the grid (Figs. 7 and 16).

Based on the 1979–2002 climatology, the NCEP/NCAR reanalysis products (Kalnay et al., 1996) indicate that an atmospheric low-pressure center is often situated over the WAP in January, consistent with the observation that during this time low-pressure systems move into this area where they subsequently decay (e.g. Turner et al., 1998). This atmospheric low-pressure center strengthens in response to La Niña and/or positive states of SAM (Fogt and Bromwich, 2006; Stammerjohn et al., 2008a). The individual January dynamic topographies (Fig. 7C) are consistent with this relationship, with the following years showing a well-developed SC: 1994 (+SAM), 1996 (weak but mutually reinforcing La Niña and +SAM), 1999 (strong La Niña and +SAM), 2000 (strong La Niña and +SAM), and 2002 (strong +SAM). In contrast, the January dynamic topography for 1995, 1998 and 2003 all show a less-developed SC but a well-developed OA, and these 3 Januaries coincided with moderate to strong El Niño events. Near-neutral ENSO and SAM Januaries were 1993, 1997 and 2001, all of which show weakened dynamic topography. Similar response patterns are apparent in chl-*a* over the broader WAP region. Klinck et al. (2004) find that their SO GLOBEC 2001 autumn and winter drifter measurements near the PAL LTER 200 line were consistent with dynamic topography (further evidence of geostrophic balance), but the weak stratification limited the baroclinic response to being only half of the total flow, so it tended to underestimate total flow by about 50%.

5.1.7. *Anomalous years*

In the cross sections of T' and S' (Fig. 5), 2002 stands out as an unusual year in the extent of anomalously warm water intruding onto the shelf (also an exceptionally penetrative incursion onto the shelf at the 300 line as indicated by the red diamonds in Fig. 7C), even as far north as the 600 line (Fig. 5B and D). An examination of the temperature anomalies relative to climatologies reveals that the 2002 incursion is more a reflection of the UCDW appearing in a shallower depth range, rather than being warmer in temperature, consistent with the previous arguments of upwelling-induced compression of the permanent pycnocline. Also, the mid-shelf cyclone in 2002 is larger than usual, its western rim extending over the continental slope, displacing the OA farther offshore (isodyns consistent with the ACC traveling tightly along the shelf break, giving more direct access to the Marguerite Trough opening at the shelf break), and extending farther up the shelf than usual. In the southern half of the gird, the correlation between the depth of T_{max} and the isodyns is particularly strong (r^2X 50%). This is consistent with Massom et al. (2006) and Turner et al. (2002) documenting the extreme nature of the cyclones hitting the region in 2002.

Noticeable shifts during our 12-year sample period are apparent in 1998 and 2002. The former is most obvious in the dramatic full-grid shift in SD_w (Fig. 12) starting in 1998. The 1998 shift happened during a period of unusually weak storm forcing (Stammerjohn et al., 2008b). Specifically, spring–autumn of 1997–1998 saw the appearance of a strong El Niño. This resulted in the equatorward shift of the polar jet (e.g., Rind et al., 2001; Yuan, 2004) resulting in weaker winds and fewer storms in the WAP region. However, in late austral autumn the winds did pick up dramatically, as the tropical Pacific transitioned into a very strong La Niña state, shifting the polar jet south, increasing the storms, and strengthening the winds as a strong low developed over the WAP (Yuan, 2004). This greatly delayed the sea-ice advance (Stammerjohn et al., 2008b), which in turn led to a short sea-ice season for the winter of 1998. However, the ocean also seems to be implicated in the low winter sea ice given that austral *summer* 1998 shows an unusually large surface heat content anomaly (Fig. 5A; in particular, note the strong warm surface anomalies on the 200 and 600 lines), requiring longer time to cool to freezing for ice formation. This is likely a result of weak winds not mixing the cold WW water into the surface layer and vertical compression of the pycnocline resulting from the largest UCDW incursion on the shelf with enhanced upwelling (producing a thicker layer) of UCDW. This has the following impacts: decreased TB_w with the thinner thermocline and decreased SD_w with a thinner and less-fresh surface layer, resulting in a negative shift in bulk stability, making entrainment easier, with elevated F_{ET}. The reason for the large incursion is unknown, though an ACC meander is not unlikely given the dramatic shift in the polar jet with the onset of the large La Niña (Yuan, 2004).

Following 1998, storm forcing becomes high during MAM when sea ice is advancing over the next 4 years (MAM 99, 00, 01, 02) in response to La Niña and/or +SAM events (see Table 1 in Stammerjohn et al., 2008b). 2001–2002 displayed the highest storm forcing measured in the region (Massom et al., 2006), manifesting itself in the ocean with the unusually large ocean heat content (4.4σ in Q_{shelf}; Fig. 10). Greater delays in the sea-ice advance are observed over these four seasons (the first early advance is observed in the autumn of 2002, immediately after the intense storm period from 1 September to 2 February), and thus shorter sea-ice seasons coincide with the overall trend towards increased Q_{shelf}—simply put: more ocean heat, less sea ice. These responses are clearly visible in our integrated heat content from the WW to the surface, or our thermal insulation, TI, available at http://www.pal.lternet.edu, following the links to the Lamont web page.

The 2002 anomaly is most apparent through an unusually large ocean heat content on the shelf (Q_{shelf}): specifically in Figs. 10A, and both parts of Fig. 14. Interestingly, the shift in 1998 is quite different from the enormous anomaly in 2002. It appears that the quiet 1998 summer reduced the amount of WW mixed to the surface via surface wind-generated turbulence leading to an

unusually warm surface layer, delaying the onset of ice growth in the 1998 autumn. This is quite different from 2002 in which the strong storms mixed considerable WW to the surface leading to a very cold summer surface layer and thus an early onset of ice growth. These changes in the atmosphere lead to a stronger cyclonic circulation cell (SC in Fig. 7A), with the SC geopotential height anomaly reaching a 12-year low in 2001 and 2002, consistent with intensifying upwelling on the southern half of the grid where pure UCDW is clearly extensively present in the Marguerite Trough. Consistent with this is the large Q_{shelf}, which is clearly the consequence of strongly enhanced upwelling as evidenced in Fig. 14A.

5.2. Potential for bottom water formation

Finally, we address the interesting results of Shevenell and Kennett (2002) who find evidence of decadal cycles (periods of cold, non-renewed shelf bottom waters alternating with warmer, renewed waters) recorded in their high-resolution sediment record from Palmer Deep (near Anvers Island). While HSSW and other dense bottom water are absent in the present day, we consider another means of forming shelf bottom water: water-column destabilization and overturn (as happened in the Weddell gyre in the early 1970s; Martinson et al., 1981). Overturn and subsequent polynya formation occur when sea-ice growth rejects enough brine to overcome the bulk stability (Martinson and Iannuzzi, 1998). A single winter's cooling could drive overturn during a year with an anomalously low R (given the observed variability over our 12 years; such might be expected near Anvers Island sometime in the next decade or two). Regardless, the bulk stability shows decreasing trends nearly ubiquitously across the entire grid, with rates decreasing as fast as 0.3 m per year in the center of the grid and near the outer edge of the shelf off of Anvers Island. Currently, the amount of bulk stability eliminated in a typical winter (with 5 months of winter surface cooling at an average rate of $\bar{F}_{air} = 32{:}5\,W\,m^{-2}$) is $\sim 1.4\,m\,y^{-1}$. For those regions with R decreasing most rapidly, $\bar{\Sigma} \sim 6$ m, so for 1.4 m loss each winter we require an extra 4.6 m of ice growth beyond a typical winter to achieve overturn. If the trends showing a decreased R continue, that 4.6 m buffer will be lost in 15 years. That along with the large interannual variability observed in R suggests that an overturn might be expected within the next decade or two (assuming no change in trends and variability, though at some point one would expect the trend to change as the system begins to adjust internally in an attempt to accommodate new conditions).

An overturn homogenizes the water column (forming a mixture about the same salinity as the deep water and slightly colder, thus comparable to present day HSSW), mixing the warm saltier deep water directly to the surface, melting away the overlying ice, and generating a polynya. In the Antarctic, ocean heat is vented about 20 times more effectively through open water than through an ice cover. So the presence of a polynya would vent considerable heat in winter, further fueling the convection (e.g., supply to depth) by making the salty homogenized water column colder, driving bottom-water production. Bottom water production following overturn/polynya formation requires on-shelf flow to conserve mass: a self-regulating mechanism for preventing isolation of shelf waters from the warmer slope waters for more than a decade on average. This could drive a negative feedback that limits the time an overturned water column would survive, offering a self-regulating mechanism of recovering the on-shore flow of UCDW in the absence of larger scale atmospheric shifts as required in *Shevenell* and *Kennett*'s mechanism. This may also provide a more realistic means of forming bottom water in a region with deep water otherwise too warm to do so.

6. Summary

Conclusions unique to this study include:

(1) The average annual ocean heat flux (to the atmosphere) over the continental shelf shows a *decreasing* trend through time averaging $0.6\,W\,m^{-2}\,y^{-1}$. The ocean heat content over the shelf shows a linearly *increasing* trend of $2.6 \times 10^7\,J m^{-2}\,y^{-1}$. This build up of heat appears to be a consequence of increased upwelling of warm UCDW onto the shelf while a weakening of the ocean heat flux being less effective in venting the heat buildup. There is a smaller contribution (during the LTER sampling period) to this Q_{shelf} increase by a slowly warming UCDW delivered to the region via the ACC. Also, while not addressed in this study, it is possible that the increase of Q_{shelf} may lead to a considerably larger thermal head in the coastal regions available for basal glacier melting.

(2) On longer time scales, it is apparent that the UCDW has warmed considerably, as indicated by the increase in Q_{slope} of the source waters as seen when comparing the historical values to the LTER sample year values (not shown was the very strong relationship between Q_{shelf} and Q_{slope}, with $r^2 = 0.77$, showing that Q_{slope} is an excellent proxy for the heat reaching the continental shelf). This longer time scale increase coincides with the strong atmospheric warming on the AP (large jump in the p 1990 years relative to the 4 1990 years; and linear trend throughout most of the LTER sampling period). We speculate that the increase in Q_{shelf} in the decades preceding our sampling, followed by only a minor change during our sample period may reflect an internal adjustment as the system attempts to transition to a new state, though we have no direct evidence of this.

(3) We compute an optimal turbulent diffusivity coefficient, required to cool the freshly trapped WW at winter's end to observed values during sampling. The estimated k_z values reflect classic open-ocean discrepancies between large-scale property-based estimates and molecular-based estimates (with the former typically being an order of magnitude larger or so). Here too, our multi-annual average k_z is $\sim 8.5 \times 10^{-5}\,m^2\,s^{-1}$; nearly an order of magnitude larger than the shear-instability-based estimates of Howard et al. (2004) value of p $1 \times 10^{-5}\,m^2 s^{-1}$. More importantly, our estimates show a systematic decrease in k_z as a function of year. Employing the annual-average value for each year, instead of a single multi-year average value, results in a dramatic change in the estimation of the ocean heat flux and its temporal evolution (something we are considering in a separate study).

(4) Year 1998 was an anomalous year on the continental shelf, showing a dramatic regime shift in a number of properties, though most notably the salt content of the deep water across the entire grid comparable to the extraction of nearly 50 cm of sea ice (a 40% shift relative to climatology). Spring-to-autumn 1998–1999 displayed a large La Niña, amplified by a strong positive SAM, and was preceded by the largest observed El Niño event in the instrumented record; numerous studies (e.g. Smith et al., 1996; Yuan and Martinson, 2001) have documented the large influence ENSO events have on the WAP area.

(5) Year 2002 was also an anomalous year on the continental shelf, showing an unusually large UCDW incursion across the shelf over the entire length of the grid, resulting in a

remarkable 4.5σ excursion in shelf heat content and an unusually large salinity anomaly. Unlike the 1998 response that shifted the entire grid for all of the following years as well, the 2002 event was limited primarily to that particular year (influenced by a weak La Niña, but amplified by a strong positive SAM).

(6) WAP water masses are well separated according to bathymetrically controlled features (i.e. continental slope, shelf and coastal sub-regions) that show consistent relationships in their shape in T–S space.

(7) Surface ocean anomalies (water above the WW to the surface relative to climatology) in T and S show similar lateral property gradients when moving from the slope toward the coast; the property gradients are comparable for each year (suggesting the mixing of two end-member water masses) resulting in a near-constant T:S of ~2:1. The lateral gradients are consistent with linear mixing that is proportional to the distance from the slope (i.e., incursions of UCDW toward the coast), such that the closer the incursion is to the coast, the stronger the anomaly (expected given the larger contrast between the slope water properties and the more coastal waters).

(8) Additional findings, noted or hypothesized previously by others (as referenced in the body of the paper), but corroborated or confirmed here given the 12 consecutive years of observations:

(9) As noted in previous studies (but only documented recently with current meter observations during SO GLOBEC), the shelf is flooded by UCDW, and this water mass provides heat and nutrients to the WAP.

(10) The most notable missing water masses in the WAP region are high- and low-salinity shelf water, fundamental ingredients of Antarctic bottom water. This is not surprising given the strong presence of the ACC that bathes the shelf in warm UCDW. However, given continuation of current trends in the bulk stability and its interannual variability, it is possible to have an overturn of the water column (with accompanying polynya and bottom water formation) within one or two decades in the Palmer Deep region near Anvers Island.

(11) The poleward limit of the ACC, defined by the poleward limit of the UCDW (and here, apparent as the Southern ACC Front (SACCF)), lies consistently, year-after-year, at the continental shelf break. Thus, this region is more susceptible to ACC influence than other regions around the Antarctic where the ACC is well removed from the shelf, typically by a polar gyre.

(12) The UCDW provides considerable ocean sensible heat to the waters below the mixed layer on the continental shelf, delivered to the shelf from the slope in response to increased upwelling over the shelf, predominantly in the southern half of the grid, where this forcing is most consistent through time.

(13) The distribution of ACC-core UCDW on the shelf in individual years (Fig. 6) is consistently limited to the canyons, suggesting that the mixing involved with encountering the canyon walls to enter the shelf floor appears to mix the pure signal out. However, the rise to the floor at the northern end of Marguerite Trough allows pure UCDW to intrude on the mid-shelf regions during some years, delivering more heat and nutrients to shallower depths, near Lavoisier Island and the southern end of Renaud Island.

(14) The geostrophic flow field for each of the 12 years shows a rather consistent, but complex, circulation field on the shelf; there are circulation cells in the southern and northern thirds of the sampling domain, with either a circulation cell or cross-shelf flow in the middle of the domain at Renaud and Lavoisier islands.

6.1. Future needs

It is abundantly clear that we are in desperate need of the surface energy budget to help interpret observations, force models, etc. Without a good observation of F_{air}, we can only guess how the surface forcing has changed with the climate warming, something that seriously limits analyses and model forecasts of future change.

The results of this study suggest that the relationship between the ACC and the WAP shelf is critical to the physical characteristics of the water column and ocean-ice interaction of the grid domain. Anomalies seem to clearly follow large-scale forcings (e.g., ENSO events and SAM strength; La Niña and +SAM leading to more upwelling of UCDW on the shelf). Grid-wide meteorological and continuous monitoring measurements are required to determine the details of the UCDW delivery to the shelf (nature of delivery, episodic or continuous, frequency and paths of intrusions). Finally, we need to better understand the relationship between Marguerite Bay and the remainder of the domain, as its influence in the south and near the coastal Islands is undeniable; sensitivities and feedbacks between the domain proper and Marguerite Bay have not been considered here. Since the ACC first encroaches upon the continental shelf further south in the Amundsen Sea, it is possible that the WAP system observed here is an analog to the processes occurring near Pine Island Glacier, where glacial melt is most extreme.

Acknowledgments

PAL LTER (WMVIMS #518603/1247) and GLOBEC (OPP-99-10122) NSF grants. This research was leveraged by support under the Cooperative Institute for Climate Applications Research (CICAR) Award no. NA03OAR4320179 from the National Oceanic and Atmospheric Administration, US Department of Commerce. The statements, findings, conclusions and recommendations are those of the author(s) and do not necessarily reflect the views of the National Oceanic and Atmospheric Administration or the Department of Commerce, and in part by a Ford Environmental Science Grant. Thanks to Arnold Gordon for comments on the T–S plots and naming of water masses, Stan Jacobs and Claudia Giulivi for numerous discussions and Ross Sea salinity anomaly data, all PAL LTER team members were helpful in discussions and comments, and to an anonymous reviewer suggesting the possible shallow cyclone of Marguerite Bay as a possible response to the freshwater input from the coast overlying a deeper anticyclone; SO GLOBEC colleagues, especially Robert Beardsley and Carlos Moffat; members of Antarctic Support Associates, and more recently Raytheon Polar Services Inc. along with captains and crews of the R.V. *IB*, L.M. Gould and N.B. Palmer, who have successfully, safely and with good humor entertained nearly all of our requests for acquiring our samples on a regular basis for the length of the program, including a number of winter and other seasonal periods. This is Lamont-Doherty Earth Observatory contribution number 7184; and PAL LTER contribution number: 0307.

References

Anderson, J.B., 2002. Antarctic Marine Geology. Cambridge University Press, Cambridge, UK.

Barnett, T.P., Pierce, D.W., Shnur, R., 2001. Detection of anthropogenic climate change in the world's oceans. Science 292, 270–274.

Beardsley, R.C., Limeburner, R., Owens, W.B., 2004. Drifter measurements of surface currents near Marguerite Bay on the western Antarctic Peninsula shelf during austral summer and fall, 2001 and 2002. Deep-Sea Research II 51, 1947–1964.

Buell, C.E., 1975. The topography of empirical orthogonal functions. In: Preprint of Fourth Conference on Prob. and Stat. in Atmos. Sci. Amer. Meteor. Soc., Tallahassee, FL, pp. 188–193.
Buell, C.E., 1979. On the physical interpretation of empirical orthogonal functions. In: Preprint of Sixth Conference on Prob. and Stat. in Atmos. Sci. Amer. Meteor. Soc., Banff, Alta., pp. 112–116.
Cane, M.A., Zebiak, S.E., Dolan, S.C., 1986. Experimental forecasts of El-Niño. Nature 321 (6073), 827–832.
Carmack, E.C., 1977. Water characteristics of the Southern Ocean south of the Polar Front. In: Angel, E. (Ed.), A Voyage of Discovery. Pergamon Press, New York, pp. 15–42.
Comiso, J.C., 1995. SSMI Ice Concentrations Using the Bootstrap Algorithm NASA RP 1380. NASA, Washington, DC, 50pp.
Comiso, J.C., 1995. Sea-ice geophysical parameters from SMMR and SSMI data. In: Ikeda, M., Dobson, F. (Eds.), Oceanographic Applications of Remote Sensing. CRC Press Inc., Boca Raton, FL, pp. 321–338.
Comiso, J.C., Cavalieri, D., Parkinson, C., Gloerson, P., 1997. Passive microwave algorithms for sea ice concentration: a comparison of two techniques. Remote Sensing of Environment 60 (3), 357–384.
Cook, A.J., Fox, A.J., Vaughan, D.G., Ferrigno, J.C., 2005. Retreating glacial fronts on the Antarctic Peninsula over the past half-century. Science 308, 541–544.
Deacon, G.E.R., 1937. The hydrology of the Southern Ocean. Discovery Reports 15, 1–124.
Dierssen, H.M., Vernet, M., Smith, R.C., 2000. Optimizing models for remotely estimating primary production in Antarctic coastal waters. Antarctic Science 12 (1), 20–32.
Dierssen, H.M., Smith, R.C., Vernet, M., 2002. Glacial meltwater dynamics in coastal waters west of the Antarctic Peninsula. Proceedings of the National Academy of Sciences 99 (4), 1790–1795.
Dinniman, M.S., Klinck, J.M., 2004. A model study of circulation and cross-shelf exchange on the west Antarctic Peninsula continental shelf. Deep-Sea Research II 51, 2003–2022.
Fahrbach, E., Meyer, R., Rohardt, G., Schroder, M., Woodgate, R.A., 1998. Gradual warming of the Weddell Sea Deep and Bottom Water, Filchner-Ronne ice shelf program. In: Filchner-Ronne Ice Shelf Program. Alfred-Wegener-Institut, Bremerhaven, Germany, pp. 24–34 (Report no. 12).
Fogt, R.L., Bromwich, D.H., 2006. Decadal variability of the ENSO teleconnection to the high latitude South Pacific governed by coupling with the Southern Annular Mode. Journal of Climate 19, 979–997.
Garibotti, I.A., Vernet, M., Kozlowski, W.A., Ferrario, M.E., 2003. Composition and biomass of phytoplankton assemblages in coastal Antarctic waters: a comparison of chemotaxonomic and microscopic analyses. Marine Ecology Progress Series 247, 27–42.
Garibotti, I.A., Vernet, M., Smith, R.C., Ferrario, M.E., 2005. Interannual variability in the distribution of the phytoplankton standing stock across the seasonal sea-ice zone west of the Antarctic Peninsula. Journal of Plankton Research 27 (8), 825–843.
Gill, A.E., 1973. Circulation and bottom water production in the Weddell Sea. Deep-Sea Research 20, 111–140.
Gille, S.T., 2002. Warming of the Southern Ocean since the 1950s. Science 295, 1275–1277.
Giulivi, C.F., Jacobs, S.S., 1997. Oceanographic Data in the Amundsen and Bellingshausen Sea. Lamont-Doherty Earth Observatory, Palisades, NY, Technical Report #LDEO-97-03, 330pp.
Gordon, A.L., 1971a. Oceanography of Antarctic waters. Antarctic Research Series 15, 169–203.
Gordon, A.L., 1971b. Antarctic polar front zone. Antarctic Research Series 15, 205–222.
Gruber, N., Sarmiento, J.L., 1997. Global patterns of marine nitrogen fixation and denitrification. Global Biogeochemical Cycles 11, 235–266.
Hall, A., Visbeck, M., 2002. Synchronous variability in the Southern Hemisphere atmosphere, sea ice, and ocean resulting from the annular mode. Journal of Climate 15, 3043–3057.
Hofmann, E.E., Klinck, J.M., 1998. Hydrography and circulation of the Antarctic continental shelf: 150°E to the Greenwich Meridian. In: Robinson, A.R., Brink, K.H. (Eds.), The Sea, vol. 11. Wiley, New York, pp. 997–1042.
Hofmann, E.E., Klinck, J.M., Lascara, C.M., Smith, D.A., 1996. Water mass distribution and circulation west of the Antarctic Peninsula and including Bransfield Strait. In: Ross, Robin M., Hofmann, Eileen E., Quetin, Langdon B. (Eds.), Foundations for Ecological Research West of the Antarctic Peninsula, Antarctic Research Series, vol. 70. American Geophysical Union, Washington, DC, pp. 61–80.
Hofmann, E.E., Klinck, J.M., Daly, K.L., Torres, J.J., Fraser, W.R., 2002. US southern ocean global ecosystems dynamics program. Oceanography: The Oceanography Society 15 (2), 64–74.
Howard, S.L., Hyatt, J., Padman, L., 2004. Mixing in the pycnocline over the western Antarctic Peninsula shelf during Southern Ocean GLOBEC. Deep-Sea Research II 51, 1965–1979.
Kalnay, E., Kanamitsu, M., Kistler, R., Collins, W., Deaven, D., Gandin, L., Iredell, M., Saha, S., White, G., Woollen, J., Zhu, Y., Chelliah, M., Ebisuzaki, W., Higgins, W., Janowlak, J., Mo, K.C., Ropelewski, C., Wang, J., Leetmaa, A., Reynolds, R., Jenne, R., Joseph, D., 1996. The NCEP/NCAR 40-year reanalysis project. Bulletin of the American Meteorological Society 77, 437–471.
Kaplan, A., Cane, M.A., Kushnir, Y., Clement, A.C., Blumenthal, M.B., Rajagopalan, B., 1998. Analyses of global sea surface temperature 1856–1991. Journal of Geophysical Research 103, 18567–18589.
King, J.C., Turner, J., Marshall, G.J., Connolly, W.M., Lachlan-Cope, T.A., 2003. Antarctic Peninsula climate variability and its causes as revealed by analysis of instrumental records. In: Domack, E., Leventer, A., Burnett, A., Bindschadler, R., Convey, P., Kirby, M. (Eds.), Antarctic Peninsula Climate Variability: Historical and Paleoenvironmental Perspectives. Antarctic Research Series, vol. 79, pp. 17–30.
Klinck, J.M., 1998. Heat and salt changes on the continental shelf west of the Antarctic Peninsula between January 1993 and January 1994. Journal of Geophysical Research, 7617–7636.
Klinck, J.M., Hofmann, E.E., Beardsley, R.C., Salihoglu, B., Howard, S., 2004. Water mass properties and circulation on the west Antarctic Peninsula continental shelf in Austral Fall and Winter 2001. Deep-Sea Research II 51 (17–19), 1925–1946.
L'Heureux, M.L., Thompson, D.W.J., 2006. Observed relationships between the El Niño–Southern Oscillation and the extratropical zonal-mean circulation. Journal of Climate 19, 276–287.
Large, W.G., Yaeger, S.G., 2004. Diurnal to decadal global forcing for ocean and sea-ice models: the data sets and flux climatologies, NCAR/TN-460+STR, NCAR Technical Note, 105pp.
Large, W., McWilliams, J.C., Donney, S.C., 1994. Ocean vertical mixing: a review and a model with a nonlocal boundary layer parameterization. Reviews of Geophysics 32 (4), 363–403.
Lefebvre, W., Goosse, H., Timmermann, R., Fichefet, T., 2004. Influence of the Southern Annular Mode on the sea ice-ocean system. Journal of Geophysical Research 109, C09005 [doi:10.1029/2004JC002403].
Liu, J., Curry, J.A., Martinson, D.G., 2004. Interpretation of recent Antarctic sea ice variability. Geophysical Research Letters 31 (L02205).
Marshall, G.J., 2003. Trends in the Southern Annular Mode from observations and reanalysis. Journal of Climate 16, 4134–4143.
Martinson, D.G., 1990. Evolution of the Southern Ocean winter mixed layer and sea ice: open ocean deepwater formation and ventilation. Journal of Geophysical Research 95, 11641–11654.
Martinson, D.G., 1991. Open ocean convection in the Southern Ocean. In: Gascard, Chu (Eds.), Deep Convection and Deep Water Formation. Elsevier Science Publishers, Amsterdam, pp. 37–52.
Martinson, D.G., Iannuzzi, R.A., 1998. Antarctic ocean-ice interaction: implications from ocean bulk property distributions in the Weddell Gyre. In: Jeffries, M. (Ed.), Antarctic Sea Ice: Physical Processes, Interactions and Variability. Antarctic Research Series, vol. 74. American Geophysical Union, Boston, pp. 243–271.
Martinson, D.G., Iannuzzi, R.A., 2003. Spatial/temporal patterns in Weddell Gyre characteristics and their relationship to global climate. Journal of Geophysical Research 108 (C4).
Martinson, D.G., Steele, M., 2001. Future of the Arctic sea ice cover: implications of an Antarctic analog. Geophysical Research Letters 28 (2), 307–310.
Martinson, D.G., Killworth, P.D., Gordon, A.L., 1981. A convective model for the Weddell polynya. Journal of Physical Oceanography ll, 466–488.
Martinson, D.G., Iannuzzi, R.A., Allspaw, S., 1999. CTD Operations Manual-RVIB Nathaniel B. Palmer. Antarctic Support Associates Technical Report.
Massom, R.A., Stammerjohn, S.E., Smith, R.C., Pook, M.J., Iannuzzi, R.A., Adams, N., Martinson, D.G., Vernet, M., Fraser, W.R., Quetin, L.B., Ross, R., Massom, Y., Roy Krouse, H., 2006. Extreme anomalous atmospheric circulation in the West Antarctic Peninsula Region in austral spring and summer 2001/02, and its profound impact on sea ice and biota. Journal of Climate 19, 3544–3571.
McPhee, M.G., Ackley, S.F., Guest, P., Huber, B.A., Martinson, D.G., Morison, J.H., Muench, R.D., Padman, L., Stanton, T.P., 1996. The Antarctic Zone flux experiment. Bulletin of the American Meteorological Society 77 (6), 1232.
McPhee, M.G., Kottmeier, C., Morison, J.H., 1999. Ocean heat flux in the Central Weddell Sea during winter. Journal of Physical Oceanography 29, 1166–1179.
Mellor, G.L., Yamada, T., 1982. Development of a turbulence closure model for geophysical fluid problems, *Rev.* Geophys. 20, 851–875.
Meredith, M.P., King, J.C., 2005. Rapid climate change in the ocean west of the Antarctic Peninsula during the second half of the 20th century. Geophysical Research Letters 32.
Moffat, C., Beardsley, R., Limeburner, R., Owens, B., Hyatt, J., 2005. Southern Ocean GLOBEC Moored array and automated weather station data report. WHOI Tech. Report WHOI-2005-07, 134pp.
Moffat, C., Beardsley, R., Owens, B., van Lipzig, N., 2008. A first description of the Antarctic Peninsula Coastal Current. Deep-Sea Research II 55, 277–293.
Montgomery, R.B., 1958. Water characteristics of Atlantic Ocean and of World Ocean. Deep-Sea Research 5, 134–148.
Mosby, H., 1934. The waters of the Atlantic Antarctic Ocean. Scientific results of the Norwegian Antarctic Expeditions 1927–1928, Nos. 10–11, pp. 117 (English translation).
Orsi, A.H., Whitworth III, T., 2005. Hydrographic atlas of the World Ocean Circulation Experiment (WOCE). In: Sparrow, M., Chapman, P., Gould, J. (Eds.), Vol. 1: Southern Ocean. International WOCE Project Office, Southampton, UK.
Orsi, A.H., Whitworth, T., Nowlin, W.D., 1995. On the meridional extent and fronts of the Antarctic Circumpolar Current. Deep-Sea Research I 42 (5), 641–673.
Pacanowski, R.C., Philander, S.G.H., 1981. Parameterization of vertical mixing in numerical models of tropical oceans. Journal of Physical Oceanography 11, 1443–1451.
Parkinson, C.L., 2002. Trends in the length of the Southern Ocean Sea Ice Season, 1979–1999. Annals of Glaciology 34, 435–440.
Parkinson, C.L., 2004. Southern Ocean sea ice and its wider linkages: insights revealed from models and observations. Antarctic Science 16 (4), 387–400.

Reid, J.L., Nowlin Jr., W.D., Patzert, W.C., 1977. On the characteristics and circulation of the Southwestern Atlantic Ocean. Journal of Physical Oceanography 7, 62–91.
Richman, M.B., 1986. Rotation of principal components. Journal of Climatology 6, 293–335.
Rind, D., Chandler, M., Lerner, J., Martinson, D.G., Yuan, X., 2001. Climate response to basin-specific changes in latitudinal temperature gradients and implications for sea ice variability. Journal of Geophysical Research V106, 20161–20173.
Robertson, R., Visbeck, M., Gordon, A., Fahrbach, E., 2002. Long-term temperature trends in the deep waters of the Weddell Sea. Deep-Sea Research II 49, 4791–4806.
Sarmiento, J.L., Gruber, N., Brzezinski, M.A., Dunne, J.P., 2004. High-latitude controls of thermocline nutrients and low latitude biological productivity. Nature V427, 56–59.
Shevenell, A.E., Kennett, J.P., 2002. Antarctic Holocene climate change: A benthic foraminiferal stable isotope record from Palmer Deep. Paleoceanography 17 (2).
Smith, D.A., Klinck, J.M., 2002. Water properties on the west Antarctic Peninsula continental shelf: a model study of effects of surface fluxes and sea ice. Deep-Sea Research II 49 (21), 4863–4886.
Smith, R.C., Stammerjohn, S.E., 2001. Variations of surface air temperature and sea ice extent in the western Antarctic Peninsula (WAP) region. Annals of Glaciology 33, 493–500.
Smith, R.C., Booth, C.R., Starr, J., 1984. Oceanographic bio-optical profiling system. Applied Optics 23, 2791–2797.
Smith, R.C., Stammerjohn, S.E., Baker, K.S., 1996. Surface air temperature variations in the western Antarctic Peninsula region. In: Ross, R.M., Hofmann, E.E., Quetin, L.B. (Eds.), Foundations for Ecological Research West of the Antarctic Peninsula. Antarctic Research Series, vol. 70. American Geophysical Union, Washington, DC, pp. 105–121.
Smith, R.C., Baker, K.S., Stammerjohn, S.E., 1998a. Exploring sea ice indices for polar ecosystem studies. BioScience 48, 83–93.
Smith, R.C., Baker, K.S., Vernet, M., 1998b. Seasonal and interannual variability of phytoplankton biomass west of the Antarctic Peninsula. Journal of Marine Systems 17 (1-4), 229–243.
Smith, R.C., Martinson, D.G., Stammerjohn, S.E., Iannuzzi, R.A., Ireson, K., 2008. Bellingshausen and Western Antarctic Peninsula Region: pigment biomass and sea ice spatial/temporal distributions and interannual variability. Deep-Sea Research II, this issue [doi:10.1016/j.dsr2.2008.04.027].
Smith, R.C., Baker, K.S., Fraser, W.R., Hofmann, E.E., Karl, D.M., Klinck, J.M., Quetin, L.B., Prezelin, B.B., Ross, R.M., Trivelpiece, W.Z., Vernet, M., 1995. The Palmer LTER: a long-term ecological research program at Palmer Station, Antarctica. Oceanography 8 (3), 77–86.
Stammerjohn, S.E., Smith, R.C., 1997. Opposing Southern Ocean climate patterns as revealed by trends in regional sea ice coverage. Climatic Change 37, 617–639.
Stammerjohn, S.E., Drinkwater, M.R., Smith, R.C., Liu, X., 2003. Ice–atmosphere interactions during sea-ice advance and retreat in the western Antarctic Peninsula region. Journal of Geophysical Research 108 (C10).
Stammerjohn, S.E., Martinson, D.G., Smith, R.C., Yuan, X., Rind, D., 2008a. Trends in Antarctic annual sea ice retreat and advance and their relation to El Nino-Southern Oscillation and Southern Annular Mode variability. J. Geophys. Res. 113, C03S90 [doi:10.1029/2007JC004269].
Stammerjohn, S.E., Martinson, D.G., Smith, R.C., Iannuzzi, R.A., 2008b. Sea ice in the Western Antartic Peninsula region: spatio–temporal variability from ecological and climate change perspectives, Deep-Sea Research II, this issue [doi:10.1016/j.dsr2.2008.04.026].
Sverdrup, H.U., 1933. On vertical circulation in the ocean due to the action of the wind with application to conditions within the Antarctic Circumpolar Current. Discovery Reports VII, 139–170.
Thompson, D.W.J., Wallace, J.M., Hegerl, G.C., 2000. Annular modes in the extratropical circulation. Part II: Trends. Journal of Climate 13, 1018–1036.
Thompson, D.W., Solomon, J.S., 2002. Interpretation of recent Southern Hemisphere climate change. Science 296, 895–899.
Tomczak, M., Large, D., 1989. Optimum multiparameter analysis of mixing in the thermocline of eastern Indian Ocean. Journal of Geophysical Research 94, 16141–16149.
Toole, J.M., 1981. Sea ice, winter convection, and the temperature minimum layer in the Southern Ocean. Journal of Geophysical Research 86, 8037–8047.
Turner, J., Marshall, G.J., Lachlan-Cope, T.A., 1998. Analysis of synopticscale low pressure systems within the Antarctic Peninsula sector of the circumpolar trough. International Journal of Climatology 18, 253–280.
Turner, J, Harangozo, S.A., Marshall, G.J., King, J.C., Colwell, S.R., 2002. Anomalous atmospheric circulation over the Weddell Sea, Antarctica, during the austral summer of 2001/02 resulting in extreme sea-ice conditions. Geophysical Research Letters 29, 2160 [doi:10.1029/2002GL015565].
Turner, J., Lachlan-Cope, T.A., Colwell, S., Marshall, G.J., Connolley, W.M., 2006. Significant warming of the Antarctic winter troposphere. Science 311, 1914–1917.
Vaughan, D.G., Marshall, G.J., Connolley, W.M., Parkinson, C., Mulvaney, R., Hodgson, D.A., King, J.C., Pudsey, C.J., Turner, J., 2003. Recent rapid regional climate warming on the Antarctic Peninsula. Climatic Change 60, 243–274.
White, W.B., Peterson, R.G., 1996. An Antarctic circumpolar wave in surface pressure, wind, temperature and sea-ice extent. Nature 380, 699–702.
Worthington, L.V., 1981. The water masses of the world: some results of a fine-scale census, in evolution of physical oceanography. In: Warren, B.A., Wunsch, C. (Eds.), Evolution of Physical Oceanography. MIT Press, Cambridge, MA, pp. 42–69.
Wust, G., 1933. Das bodenwasser und die Gliederung der Atlantischen Tiefsee. Wissenschaftliche Ergebnisse der Deutschen Atlantischen Expedition auf dem Fourschungs und Vormessungsschiff Meteor 1925–1927 6 (1), 106.
Yuan, X., 2004. Extra-polar climate impacts on Antarctic sea ice: phenomenon and mechanisms. Antarctic Science 16 (4), 415–425.
Yuan, X., Martinson, D.G., 2000. Antarctic sea ice extent variability and its global connectivity. Journal of Climate 13, 1697–1717.
Yuan, X., Martinson, D.G., 2001. The Antarctic dipole and its predictability. Geophysical Research Letters 28 (18), 3609–3612.